Check for updates

Carbon-based materials for photo- and electrocatalytic synthesis of hydrogen peroxide

Xiaoyi Hu, Xiangkang Zeng, Yue Liu, Jun Lu and Xiwang Zhang (iD) *

The high demand for hydrogen peroxide (H_2O_2) has been dominantly supplied by the anthraquinone process for various applications globally, including chemical synthesis and wastewater treatment. However, the centralized manufacturing and intensive energy input and waste output are significant challenges associated with this process. Accordingly, the on-site production of H_2O_2 *via* electro- and photocatalytic water oxidation and oxygen reduction partially is greener and easier to handle and has recently emerged with extensive research aiming to seek active, selective and stable catalysts. Herein, we review the current status and future perspectives in this field focused on carbon-based catalysts and their hybrids, since they are relatively inexpensive, bio-friendly and flexible for structural modulation. We present state-of-the-art progress, typical strategies for catalyst engineering towards selective and active H_2O_2 production, discussion on electro- and photochemical mechanisms and H_2O_2 formation through both reductive and oxidative reaction pathways, and conclude with the key challenges to be overcome. We expect promising developments would be inspired in the near future towards practical decentralized H_2O_2 production and its direct use.

1. Introduction

Along with the rapid advances of society, the unsustainability of fossil fuels as the main energy source and the resulting environmental disruption arouse pressing needs for alternative

Department of Chemical Engineering, Monash University, Clayton, VIC 3168, Australia. E-mail: xiwang.zhang@monash.edu

energy sources and green solutions. Hydrogen peroxide (H_2O_2) is an important green chemical that has illustrated great application potentials in many fields[1,2] as a clean oxidant in the paper industry,[3–5] wastewater treatment,[6,7] disinfection[8–11] and chemical synthesis,[12–15] and as a promising energy carrier in fuel cells.[16–18] The advantages of having the highest concentration of active oxygen (47.1 wt%) and producing the cleanest by-product (H_2O) make H_2O_2 particularly appealing amongst

Xiaoyi Hu is currently a Ph.D. candidate in the Department of Chemical Engineering at Monash University under the supervision of Prof. Xiwang Zhang. She received her M.S. Degree in Materials Science from Xiamen University, China, in 2014. Her current research focuses on the synthesis of carbon-based catalyst materials for solar-driven oxidation and water treatment.

Xiaoyi Hu

Xiwang Zhang is a Professor in the Department of Chemical Engineering at Monash University, and the Director of ARC Research Hub for Energy efficient Separation. His research interests focus on membrane and advanced oxidation technologies. Prof. Zhang was the recipient of the prestigious Australian Research Fellowship and Larkins Fellowship. Prof. Zhang has authored more than 160 peer-reviewed journal papers, including Nature Materials, Energy & Environmental Science, Science Advances, Nature Communications, Advanced Materials, J. Am. Chem. Soc, Advanced functional materials, Angew. Chem. Int. Ed., and ACS Catalysis.

Xiwang Zhang

various oxidants.[19] Currently, over 95% of H_2O_2 is produced industrially *via* the mature anthraquinone (AQ) process, consisting of a four-step cycle[19] (Fig. 1a): (i) hydrogenation of AQ, (ii) oxidation of hydrogenated AQ to regenerate it and yield H_2O_2, (iii) extraction-purification-concentration of H_2O_2 and (iv) reclaiming the working solutions. However, although the H_2O_2 yield is high in this large-scale synthetic process, it involves intensive energy input and chemical waste output. Furthermore, side reactions (Fig. 1a-v) produce organic by-products and consume AQ when the aromatic ring is hydrogenated, and consequently AQ cannot be recovered fully during this cycling process. Moreover, there are safety issues associated with the storage and transportation of unstable H_2O_2 right from the centralized factory to the end users.

Considering that in many applications, only H_2O_2 diluents are required, it is unnecessary to endure the risks and energy cost associated with H_2O_2 concentration and its transpor-

tation, when it can be produced locally for on-site point of use.[21,22] The major applications including pulp bleaching and chemical synthesis require H_2O_2 concentration of less than 9 wt%. Moreover, concentrations as low as 3 wt% and 0.1 wt% are enough for many medical uses and the remediation of chemical and microbial contaminations, respectively.[23] Thus, the subsequent dilution of the high concentration H_2O_2 product (up to 70 wt%) obtained in the AQ process is required, resulting in an energy wastage. Therefore, the direct synthesis of H_2O_2 from H_2 and O_2 appear to be an alternative and the toxic by-products can be minimized without AQ as the reaction carrier (Fig. 1b).[24,25] Unfortunately, besides the expected reaction of $H_2 + O_2 \rightarrow H_2O_2$, a series of undesirable reactions such as $2H_2 + O_2 \rightarrow 2H_2O$ also occur, which are even more thermodynamically favored. However, the major challenge involves handling of the explosive gaseous mixture of H_2/O_2, which requires some inert carrier gases (such as nitrogen, carbon
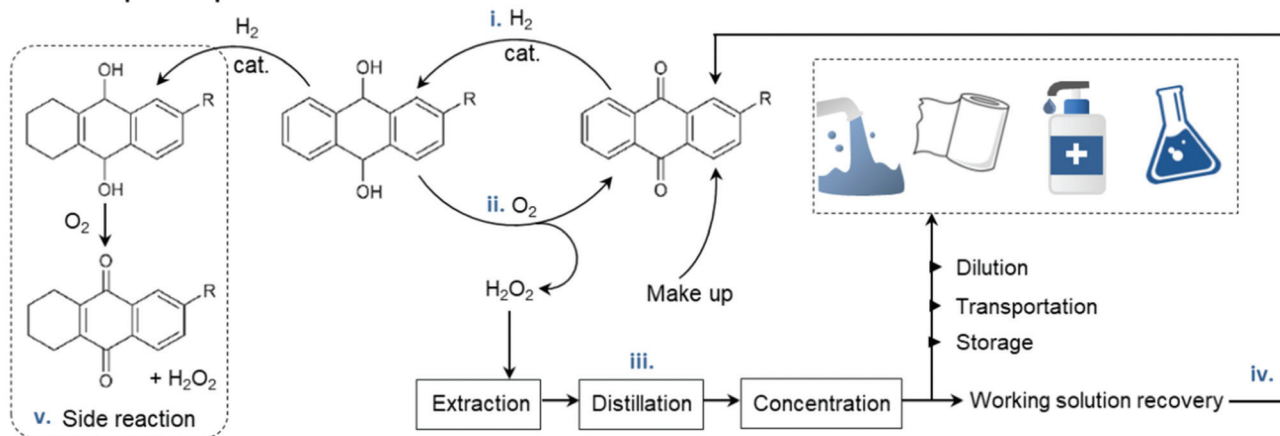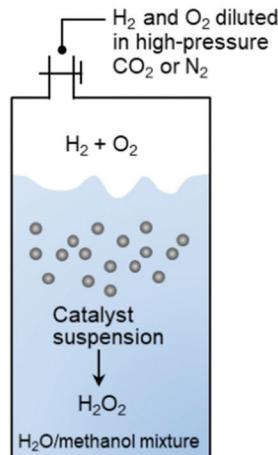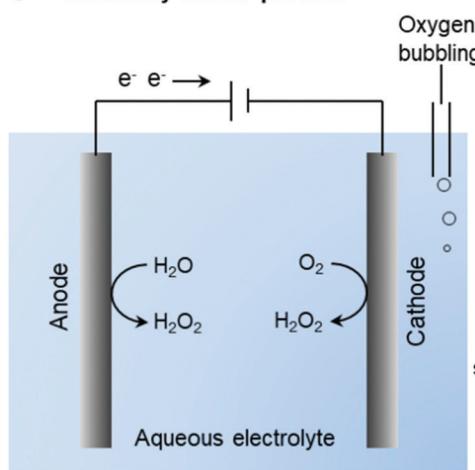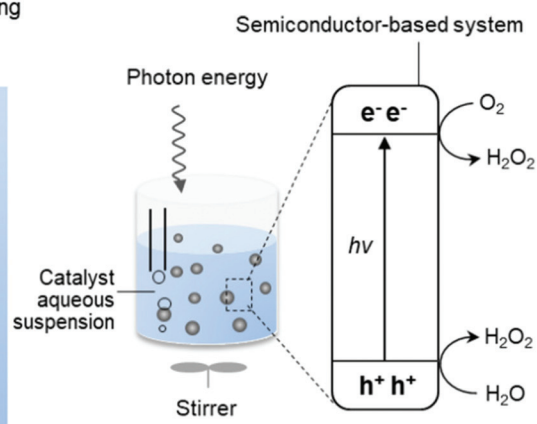
Fig. 1 Simplified schematic of the different catalytic technologies employed in the production of H_2O_2. (a) Industrialized anthraquinone process using H_2 and O_2, following a four-step cycle (i–iv), ending with various applications. Side reaction (v) consumes AQ. (b) Direct synthesis from H_2 and O_2 with inert gas carrier and mixed solvent. Adapted with permission.[20] Copyright 2019 American Association for the Advancement of Science. Decentralized (c) electrocatalysis and (d) photocatalysis from water oxidation or oxygen reduction mainly *via* a two-electron pathway.

dioxide or argon) to reduce the danger.[20] Consequently, the selectivity and productivity are partially sacrificed. To date, the expensive noble metal catalysts have been exclusively used for higher selectivity and activity in this reaction. Hence, alternative routes for the localized synthesis of H_2O_2, which are cost-effective, mild, efficient, and environmentally benign, are still in demand.

The recently emerging H_2O_2 production from water and oxygen driven by electricity (Fig. 1c) or light (Fig. 1d) has attracted significant attention.[22,26–30] Compared to the aforementioned two technologies, it is much greener and easier to handle with lower operating risks. Generally, three key factors are considered and tuned to optimize the performance of catalysts including: (i) catalyst material engineering, (ii) reaction setup, and (iii) reaction conditions (solution composition, pH, promoters, and others). In particular, the catalyst system as a critical element towards the selectivity of H_2O_2 formation has been the main focus. A wide variety of materials such as metal/metal alloys, metal oxides, carbon nanomaterials, graphene, graphitic carbon nitrides and polymer semiconductors and their hybrids have been demonstrated to be effective as electrocatalysts[31–34] and photocatalysts,[35–38] among which carbon-based materials have attracted significant interest. Much effort has been made in the design of carbon-incorporated catalyst systems for the selective and active production of H_2O_2 since they are relatively inexpensive, bio-friendly and flexible for structure modulation. Hence, this review presents the current status and future perspectives, focusing on a wide range of carbon-based catalysts. It includes the state-of-the-art progress, typical strategies for catalyst engineering towards H_2O_2 production, discussion of the electro- and photochemical mechanism and H_2O_2 formation through both reductive and oxidative reaction pathways. Finally, we also present the key challenges to be overcome towards practical decentralized H_2O_2 production and its direct use.

2. Basics in catalytic synthesis of hydrogen peroxide from water and oxygen

2.1. Oxygen reduction and water oxidation reactions

Theoretically, H_2O_2 can be formed from H_2O and O_2 *via* electrocatalysis or photocatalysis (in the presence of photoabsorbers).[28,39,40] It involves the oxygen reduction reaction (ORR) and water oxidation reaction (WOR) mainly through a two-electron ($2e^-$) pathway, which competes with the four-electron transfer towards H_2O and O_2 (possible redox pathways are summarized in Fig. 2).[28] To date, much progress has been reported for the $2e^-$ ORR, while the $2e^-$ WOR has been rarely explored until very recently. However, the possible electron transfer pathways are much more complex in the water/oxygen system. The electron-reduction of oxygen can undergo $1e^-$ (eqn (1)), $2e^-$ (eqn (2)), and $4e^-$ (eqn (3)) processes, yielding
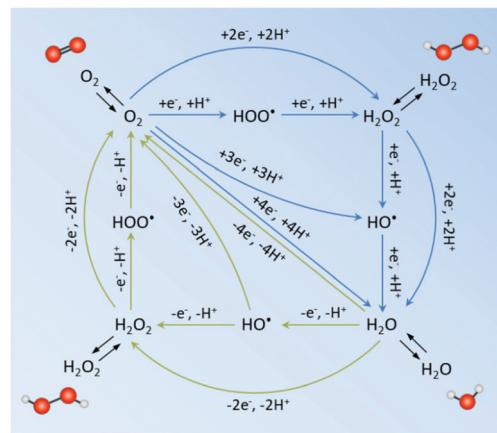
Fig. 2 Possible reduction pathways from O_2 to H_2O (blue) and oxidation pathways from H_2O to O_2 (green). The black arrows denote the adsorption and desorption/diffusion of species from the bulk solution and the catalyst. Oxygen and hydrogen atoms are represented as red and white balls, respectively. Stoichiometric H_2O is omitted for clarity.[28]

the superoxide anion $O_2^{\bullet-}$ ($^{\bullet}OOH$ is the protonated form of $O_2^{\bullet-}$), H_2O_2 and H_2O, respectively, as follows:[28]

$$O_2 + e^- \rightarrow O_2^{\bullet-} \quad E^\circ = -0.33 \text{ V } vs. \text{ RHE} \tag{1}$$

$$O_2 + 2e^- + 2H^+ \rightarrow H_2O_2 \quad E^\circ = 0.68 \text{ V } vs. \text{ RHE} \tag{2}$$

$$O_2 + 4e^- + 4H^+ \rightarrow 2H_2O \quad E^\circ = 1.23 \text{ V } vs. \text{ RHE} \tag{3}$$
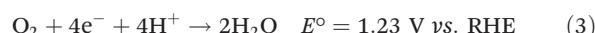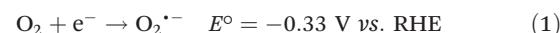
The direct $2e^-$ process and a sequential two-step $1e^-$ process are both considered feasible to produce H_2O_2, depending on how strong the intermediate OOH* (where * denotes a site on the catalyst surface) adsorbs on the catalyst surface. For example, in the case of weak OOH* adsorption, $O_2^{\bullet-}$ dissolves in the bulk solution and may undergo further reduction upon re-interaction with the active sites on the catalyst surface. On the other hand, the WOR can proceed *via* $1e^-$ (eqn (4)), $2e^-$ (eqn (5)), and $4e^-$ (eqn (6)) transfer to form hydroxyl radicals $^{\bullet}OH$, H_2O_2 and O_2 as follows:[39]

$$H_2O \rightarrow {}^{\bullet}OH + e^- + H^+ \quad E^\circ = 2.73 \text{ V } vs. \text{ RHE} \tag{4}$$

$$2H_2O \rightarrow H_2O_2 + 2e^- + 2H^+ \quad E^\circ = 1.76 \text{ V } vs. \text{ RHE} \tag{5}$$

$$2H_2O \rightarrow O_2 + 4e^- + 4H^+ \quad E^\circ = 1.23 \text{ V } vs. \text{ RHE} \tag{6}$$
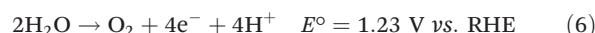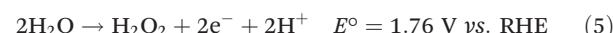
Similarly, the adsorption energies of the intermediates for the $1e^-$ and $2e^-$ WOR (*i.e.* OH* and O*) are key factors that influence the following steps to be the dissociation of OH* to form $^{\bullet}OH$, or further oxidation to H_2O_2 or H_2O. More complexity arises from the undesirable decomposition of H_2O_2 through spontaneous disproportionation ($2H_2O_2 \rightarrow 2H_2O + O_2$) or homolysis ($H_2O_2 \rightarrow 2^{\bullet}OH$). Accordingly, in an electrochemical or photochemical unit, H_2O_2 can be formed *via* either reaction leading to H_2O_2 or indirect pathways.
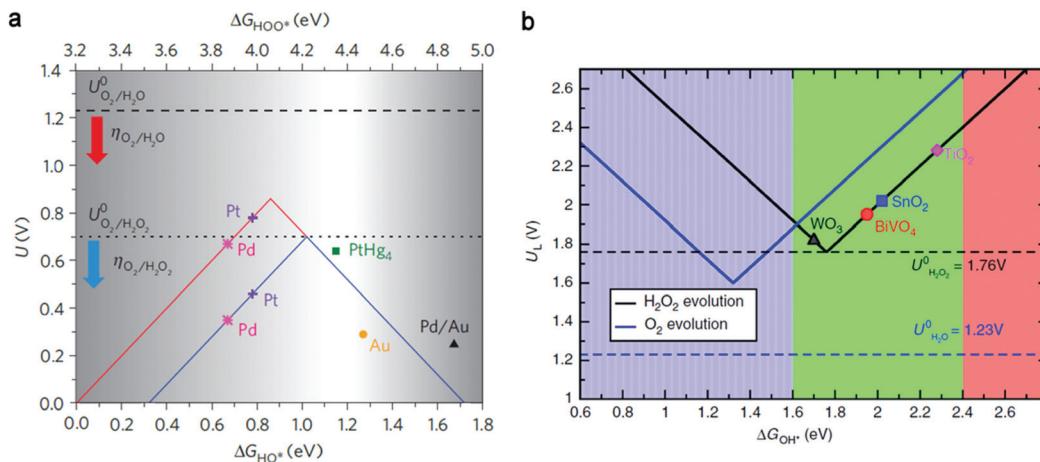
Fig. 3   (a) Calculated oxygen reduction volcano plot for the two-electron (blue) and four-electron (red) reduction of O_2, with the limiting potential plotted as a function of ΔG_{HO^*} (lower horizontal axis) and ΔG_{HOO^*} (upper horizontal axis). The equilibrium potentials for the two-electron and four-electron pathway are shown as the dotted line and dashed line, respectively. The range of interesting OH* free energy for high selectivity and activity is highlighted with the greyscale gradient at its edges, recognizing limitations to the accuracy of DFT. Reproduced with permission.[33] Copyright 2013 Springer Nature. (b) Activity volcano plots based on calculated limiting potentials as a function of calculated ΔG_{OH^*} for the two-electron oxidation of H_2O to H_2O_2 (black) and the four-electron oxidation to O_2 (blue). The corresponding equilibrium potentials for each reaction are shown in dashed lines. Reproduced with permission.[41] Copyright 2017 Springer Nature.

2.2. Selectivity and activity towards H_2O_2

Importantly, the screening of efficient and selective catalyst materials is a priority in the electrocatalytic and photocatalytic production of H_2O_2. The trends in electrochemical ORR and WOR to H_2O_2 have been theoretically predicted by density functional theory (DFT) calculations on different classes of materials including pure metals and metal alloys (Fig. 3a),[33] metal oxides (Fig. 3b),[41] and carbon-based materials,[28] with experimental supporting evidence for some. Here, we introduce briefly the fundamental theoretical basis, which is suggested to be applicable to other materials. The oxidation pathway (Fig. 3b) is taken as an example,[41] and the reduction pathway follows a similar rule. The theoretical limiting potential (U_L, the lowest potential for all reaction steps being downhill in free energy) is plotted as a function of Gibbs free energy of binding the one-electron oxidation intermediate OH* (ΔG_{OH^*}), presenting a volcano relationship. Specifically, the overpotential (denoted as the difference between U_L and equilibrium potential 1.76 V) follows the same correlation as ΔG_{OH^*}, thus the catalytic activity. The lowest overpotential (zero) at the peak of the volcano suggests a highest activity of an ideal catalyst with the ΔG_{OH^*} value located at ~1.76 eV. Otherwise, it will need certain overpotential to overcome either the uphill OH* formation (on the right hand of the peak) or the $1e^-$ reduction of OH* to H_2O_2 (on the left hand of the peak).

Regarding the selectivity towards H_2O_2, there is a suitable range for ΔG_{OH^*}, and thus the OH* binding is not too weak or too strong. Specifically, catalysts with weaker OH* are less likely to undergo $4e^-$ oxidation; however, if ΔG_{OH^*} is higher than the free energy for ·OH formation (2.4 eV), ·OH will dissolve before two-electron reduction occurs. On the other hand, O* binding should be weak enough to form H_2O_2 (with free energy of 3.5 eV) rather than undergoing further oxidation,

hence $\Delta G_{O^*} \geq 3.5$ eV. Considering the general scaling relation between ΔG_{O^*} and ΔG_{OH^*} ($\Delta G_{O^*} = 2\Delta G_{OH^*} + 0.28$), the down limit is then set to be 1.6 eV. With the range of 1.6 eV $\leq \Delta G_{OH^*} \leq 2.4$ eV, one can expect catalysts with high selectivity and activity towards H_2O_2.

Therefore, it is important to characterize the selectivity of catalysts experimentally. Currently, rotating disk electrode (RDE) analysis can be used to determine the preferred electron transfer number for electrochemical ORR.[22] A rotating ring-disk electrode (RRDE) in a three-electrode cell can further provide quantitative measurement of the produced H_2O_2 from oxygen reduction. Selectivity can be calculated in two ways, i.e. faradaic efficiency and the fraction of oxygen used to produce H_2O_2. However, some researchers have suggested that these analyses may have some inherent limitations, and instead, used a modified hermetically sealed electrochemical H-cell to quantitatively measure the oxygen consumption and H_2O_2 production (described as the total electrons consumed per oxygen molecule (e^-/O_2)).[34] For the water oxidation reaction, selectivity can be evaluated via the faradaic efficiency, which is defined as the ratio of charge converted to H_2O_2 to the total number of charge transferred. The above theory is generally used as reference for photochemical processes; however, the light response and separation of photogenerated electrons on the conduction band (CB) and holes (h^+) on valence band (VB) are other important factors.

3. Typical carbon-based catalysts

3.1. Polymeric carbon nitride and its hybrids

3.1.1. Features and history. Polymeric carbon nitride contains aromatic molecules with an alternating arrangement of
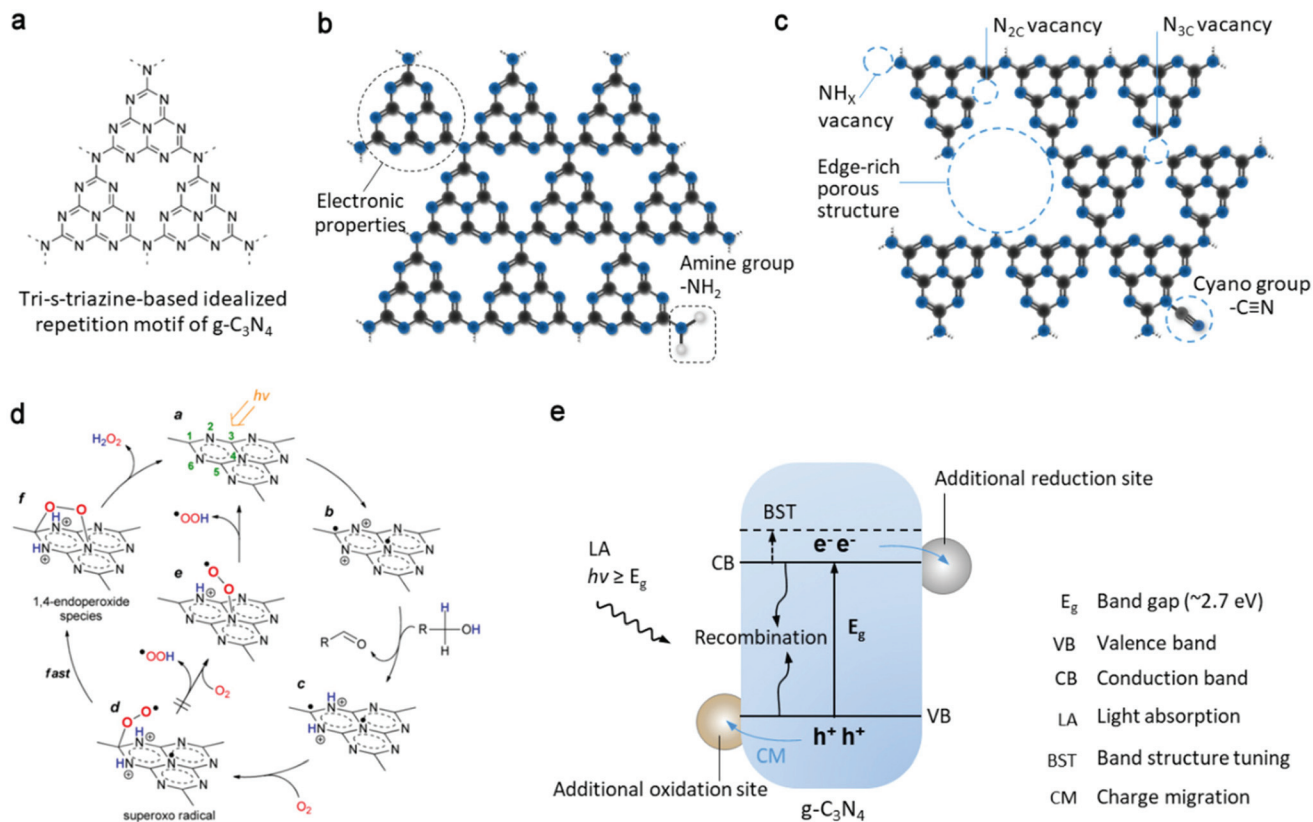
Fig. 4 (a) Tri-s-triazine structure on g-C$_3$N$_4$ sheet. (b) Intrinsic C−N aromatic rings on the g-C$_3$N$_4$ sheet define its electronic properties, rich with amine groups at the edge of g-C$_3$N$_4$. (c) Different nitrogen vacancies, concept of porous structure and cyano functional group as several possible active sites. (d) Proposed mechanism for selective H$_2$O$_2$ formation on the surface of photoactivated g-C$_3$N$_4$. Reproduced with permission.[38] Copyright 2014 American Chemical Society. (e) Photoinduced process of g-C$_3$N$_4$ semiconductor, including light absorption, generation and migration of charge carriers for surface redox reaction or recombination. Band structure tuning, additional reduction and oxidation sites (*e.g.* by modification with organic molecules, cocatalysts or other semiconductors) are some of the general approaches for the optimization of the photoactivity of g-C$_3$N$_4$.

earth-abundant carbon and nitrogen elements.[42] Carbon nitride catalysts used for the production of H$_2$O$_2$ mostly refer to a two-dimensional (2D) layered structure with heptazine rings repeating on basal planes (Fig. 4a) with van der Waals forces existing between each layer, namely graphitic carbon nitride (g-C$_3$N$_4$).[43,44] With the large amount of C replaced by N, it possesses a suitable electronic band gap (E_g) of ~2.7 eV and is responsive to light wavelength lower than ~460 nm, which makes it significantly different to semi-metallic graphene and graphite carbon with relatively higher conductivity (Fig. 4b and e). Due to its semiconductor property and unique structure featuring rich Lewis basic functions, Brønsted basic functions and H-bonding motif, g-C$_3$N$_4$ has been substantially investigated in heterogeneous photo- and electrocatalysis as a photoabsorber and catalyst (Fig. 4b).[45–48] However, the electrocatalytic production of H$_2$O$_2$ with g-C$_3$N$_4$ has been rarely reported to date far. One possible limitation hampering its future employment may be that the balance between selectivity towards the 2e⁻ ORR and sufficient overpotential to afford higher activity is difficult to achieve before a breakthrough can be made at this point.

The pioneering work[38] used g-C$_3$N$_4$ for photosynthesis of H$_2$O$_2$ and realized visible-light excitation (>420 nm) and higher selectivity (90%) compared to that of the previously reported TiO$_2$ system. According to the subsequent work by the same group, the origin of this performance is the intermediate 1,4-endoperoxide species (Fig. 4d) on the surface of g-C$_3$N$_4$, which selectively promote the two-electron ORR route (pathway is shown in Fig. 5a), whereas the peroxo species coordinated with Ti⁴⁺ on the surface of TiO$_2$ only enhance the selectivity up to 32.8%. Also, the decomposition decreased in the absence of ultraviolet range irradiation. However, their findings greatly depended on the oxidation half-reaction of alcohols (such as benzyl alcohol or ethanol) on the photogenerated h⁺ side, which provides protons and electrons for the reduction of O$_2$ to H$_2$O$_2$. Subsequently, they further demonstrated water oxidation to directly generate O$_2$ and H⁺ (eqn (6)) by modifying g-C$_3$N$_4$ with aromatic diamide[49] and graphene[50] for band structure tuning (mainly for positively shifted VB position) and electron trapping, respectively (pathway is similar to that in Fig. 5c). This solar-to-chemical reaction involving only water, O$_2$ and metal-free catalysts is particularly
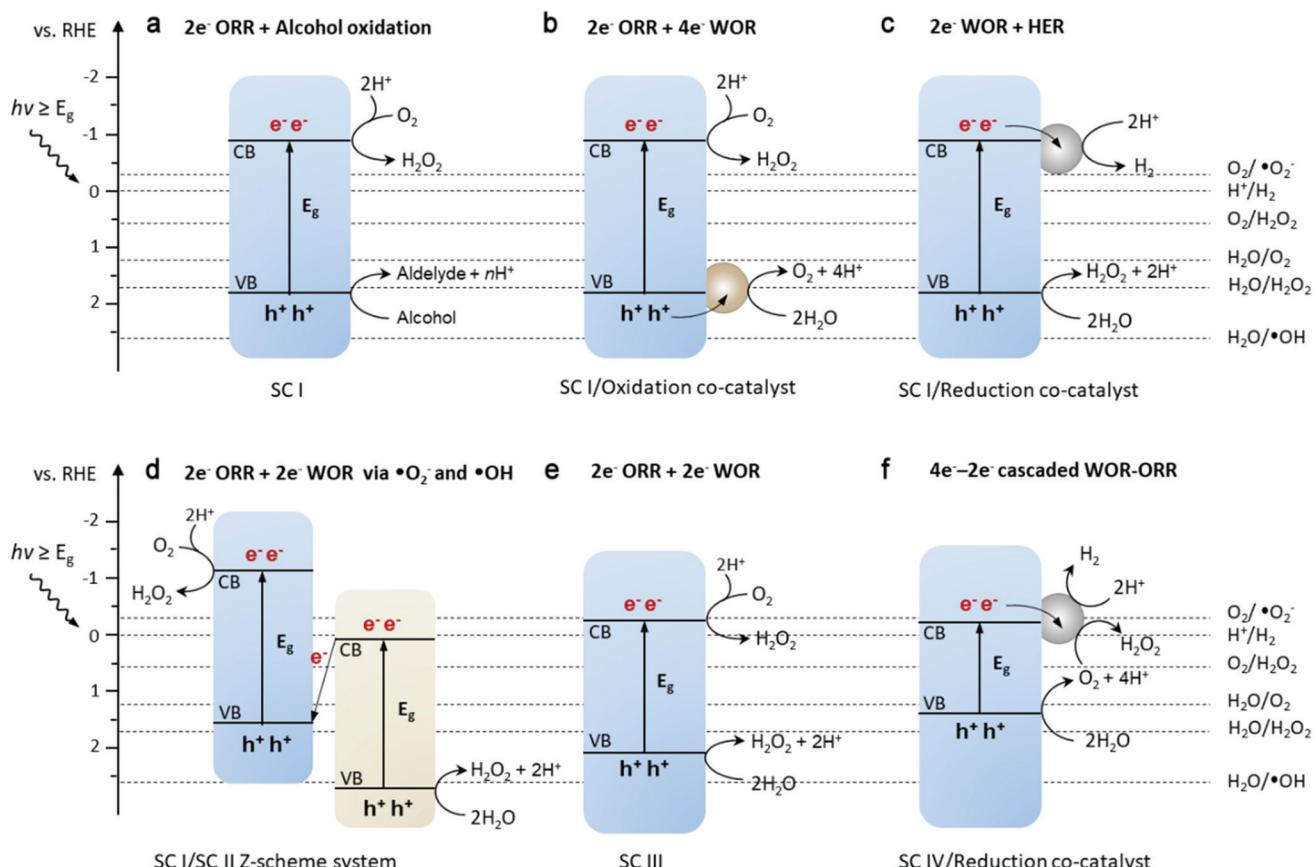
Fig. 5 Different redox pathways for photochemical H_2O_2 formation (a–f) and selected redox reaction potentials regarding the oxygen reduction reaction (ORR) and water oxidation reaction (WOR). SC and HER are abbreviations of semiconductor and hydrogen evolution reaction, respectively. SCs I–IV are different semiconductors in previously reported specific systems for the photocatalytic synthesis of H_2O_2.

promising for the cheap and sustainable on-site production of H_2O_2, paving the way for further development of g-C_3N_4-based catalysts towards higher activity and selectivity.

    3.1.2.   Modification of carbon nitride. Vacancies, additional functional groups and doped heteroatoms often result in changes in the electronic structure of the g-C_3N_4 matrix, such as shift in Fermi levels, shift in the valence/conduction orbital, and variation in density of states.[46,51–56] Thus, its photoresponse, charge migration/separation and reaction kinetics can be adjusted for potentially improving its catalytic performance.

    Due to carbon vacancies and amino group termination, g-C_3N_4 demonstrated a great improvement (by a factor of 14) in non-sacrificial oxygen reduction to H_2O_2, and altered the pathway from a sequential $1e^-$ ORR to a direct $2e^-$ ORR.[55] The reduced symmetry of g-C_3N_4 and the electron delocalization were explained as critical points for these results. Ye's group investigated how two types of nitrogen vacancies (NH_X and N_{2C}, Fig. 4c) in polymeric carbon nitride (PCN) affected the reductive formation of H_2O_2.[57] According to DFT calculation, they found a redistributed local energy level and changed Fermi level. When combining experiments with controlled vacancies, they explained that NH_X assisted charge separation,

whereas N_{2C} activated oxygen more selectively in the $2e^-$ pathway. Regarding the precise control of defects, the fabrication procedure should be considered seriously.

    The functional groups on the carbon nitride surface can directly act as catalytic active sites by regulating the adsorption of reactants and energy profile of reactions. The above mentioned KOH post-treatment of g-C_3N_4 and calcination resulted in the formation of NH_X and N_{2C} vacancies, but in another work by Tian and coauthors,[58] the one pot calcination of KOH and g-C_3N_4 precursor (urea) basically introduced cyano groups (Fig. 4c) on the N position shared by tri-s-triazine units, resulting in a different modulation of properties and catalytic optimization. The concurrent breakage of pyridine nitride and creation of –C≡N bonds were observed after annealing the g-C_3N_4 matrix under a reductive atmosphere. The resultant variation in electronic structure including deviation in electrons from melem units and new intermediate energy level led to a better photochemical performance for the generation of H_2O_2.[52] By grafting hydroxyl groups on the surface of PCN, an ultrahigh apparent quantum yield (AQY, 52.8%) was reported for the photocatalytic synthesis of H_2O_2 in ethanol solution.[59] The hydroxyl groups helped lower thermodynamic threshold for the conversion of O_2 into $O_2^{\cdot-}$ (eqn (1)) and its oxidation to

$^{\cdot}$OH could selectively oxidize ethanol to provide protons on the VB side for the subsequent reaction from $O_2^{\cdot-}$ to H_2O_2 with electron/proton transfer. Nonetheless, the activity was reduced during the recycling test because of the oxidation of the hydroxyl groups.

Modification with oxygen functional groups is one common approach in developing effective carbon-based catalysts.[54] In oxygen-rich g-C$_3$N$_4$ catalysts, the C–O–C carbon–oxygen group could greatly lower the energy of protonation of the g-C$_3$N$_4$ structure compared to –NH$_2$ and –OH groups, thus improving the ORR activity with preference for two-electron transfer, and an AQY of 10.2% was obtained at 420 nm. Recently, a simple co-polymerization of melem and barbituric acid introduced C=O groups in the carbon nitride matrix, which resulted in a positive shift in the top of VB, allowing the oxidation of H_2O to O_2 and inducing a sequential 1e$^-$ ORR with expended visible light absorption.[53] Notably, oxidized carbon was also reported to exhibit high 2e$^-$ ORR selectivity and activity using other carbon-based catalysts, for example, carbon nanotubes (CNT)[32] and graphene.[34] Thus, this approach and the disclosed mechanisms are highly recommended to be the focus of further studies.

Doping of heteroatoms may alter the reaction pathway to H_2O_2. A two-in-one strategy[60] incorporating a porous structure and phosphorous doping enabled H_2O_2 production under visible light illumination via both indirect 2e$^-$ WOR on the VB side and 2e$^-$ ORR on the CB side. The production rate (1968 μmol g^{-1} h^{-1}) recorded was among the highest for pure water photocatalytic systems driven by visible light. The authors deduced that H_2O_2 was formed by the combination of two $^{\cdot}$OH from one-electron water oxidation (eqn (4)) on the h$^+$ side and a sequential two-step single electron activation of O_2 on the e$^-$ side. In contrast, in another similar system (P doped porous g-C$_3$N$_4$ nanosheets),[61] the direct 2e$^-$ ORR was dominant due to the down-shifted bottom of the CB. Generally, the oxidation potential of the $^{\cdot}$OH/H_2O reaction is more positive than the top of the VB of pristine g-C$_3$N$_4$, and thus the detection of $^{\cdot}$OH failed for many g-C$_3$N$_4$-based catalysts (not referring to hybrid catalysts). Nevertheless, the two-channel photocatalytic synthesis of H_2O_2 is extremely attractive for practical solar-to-chemical application in the future, although more detailed mechanism studies need to be further conducted for a clear reaction pathway to H_2O_2. In addition, halogen doping was also found to be effective for the photocatalytic synthesis of H_2O_2 over g-C$_3$N$_4$ nanorods.[62] Besides, the incorporation of multiple heteroelements into PCN with other possible configurations was demonstrated by Choi's group by simple calcination of melamine in the presence of potassium salts.[63,64] The AQYs were boosted by 17–25 times in comparison to that of the unmodified carbon nitride (under monochromatic irradiation of 420 and 320 nm). The incorporation of heteroatoms (K, P, and O) was characterized by various spectroscopic methods, though it was difficulty to give the exact structure and synthetic mechanism of the modified carbon nitride, for which the building blocks are usually different from ideal theoretical models. However, due to the earth-abundant pre-

cursors and easy synthesis, this optimization route could be possibly scaled up.

To reveal the relation between the porosity and activity, Shiraishi's group[65] fabricated a group of g-C$_3$N$_4$ catalysts via the silicon-templated thermal polymerization of cyanamide. It was found that a moderate surface area showed optimized activity for H_2O_2 production. However, a further increase in surface area had a negative effect on the selectivity of g-C$_3$N$_4$ towards the 2e$^-$ ORR since the increase in the number of intrinsic amine groups in mesoporous g-C$_3$N$_4$ made it easier to drive the 4e$^-$ ORR, where the authors proposed that melem units are the active sites for selective 2e$^-$ ORR. Hence, excess defects in porous g-C$_3$N$_4$ may reduce the H_2O_2 selectivity by decreasing the amount of inherent active sites on g-C$_3$N$_4$, and accordingly a larger surface area, which is believed to decrease the charge/mass transfer and accelerate the reaction kinetics, becomes less important. Subsequently, Wang's group[66] fabricated carbon nitride aerogels via a sol–gel process by simply leaving a water suspension of carbon nitride nanoparticles to stand, which had highly exposed –NH$_X$ and hydroxyl groups to promote physical interaction forces, and thus form a hydrogel. The resulting aerogels exhibited an increased production of H_2O_2 from water and oxygen. Both the hierarchical porous structure and functional groups including –C≡N and hydrogen-containing groups synergistically contributed to the enhancement.

3.1.3. Hybridization strategy. Generally, g-C$_3$N$_4$ is coupled with other components for the purpose of (i) efficient charge separation by introducing electron traps, (ii) appropriate band alignment by constructing heterojunction or Z-scheme systems, and (iii) creation of additional active sites. Accordingly, one can modulate the charge transfer behavior, facilitate 4e$^-$ WOR towards oxygen evolution (so that the sacrificial alcohol oxidation can be replaced) and create new reaction centers.[67–70] The surface of g-C$_3$N$_4$ is negatively charged with rich functional groups (particularly exfoliated 2D g-C$_3$N$_4$ nanosheets), which as a substrate allows multiple types of interactions with metals (or metallic species), metal compounds, organic molecules, and other carbonaceous species.

The strong anchoring of metal compounds on g-C$_3$N$_4$ is attributed to the delocalization of long electrons induced by element-doping (such as P) in the g-C$_3$N$_4$ matrix. Xue et $al.$[71] found that substitutional P facilitated the binding of Co$_x$Ni$_y$P clusters onto g-C$_3$N$_4$ (Co$_x$Ni$_y$P-PCN) by P$^+$-P$^{\delta-}$-Co$^{\delta+}$/Ni$^{\delta+}$ centers. Photogenerated electrons were much favorable to be transferred to these charged centers, and subsequently the Co$_x$Ni$_y$P clusters, leaving holes on the g-C$_3$N$_4$ substrate. The calculated H binding energy on CoNiP clusters, ΔG_{H^*}, was close to zero (the top of hydrogen evolution reaction volcano plots). Hence, this catalyst system resulted in a unique water splitting route to H_2 on the CoNiP clusters and H_2O_2 on g-C$_3$N$_4$ via a direct 2e$^-$ WOR pathway (Fig. 5c). The hybridization method is also a crucial point to be considered since robust interfacial contact and uniform dispersion are widely verified to be significant, for example when loading metallic nanostructures onto g-C$_3$N$_4$. Accordingly, Cai et $al.$[72] modified ultrathin g-C$_3$N$_4$ with

the redox of dopamine *via* a one-pot polymerization to obtain a homogeneous decoration of silver (Ag@U-g-C_3N_4-NS). The activity for H_2O_2 production was improved since the Ag nanoparticles preferred photoformation of H_2O_2 over its decomposition. Meanwhile, Ag@U-g-C_3N_4-NS presented outstanding performance in the degradation of common organic pollutants, demonstrating both the application of environmental remediation and green chemical synthesis. To maximize the interfacial contact area, the 2D/2D geometry is thought helpful for a tight interface and promoted mass/charge interaction between two components.[73] Besides metal cocatalysts (which are often nanoparticles), metallic sulfides (such as MoS_2)[74] can serve as e^- acceptors and additional active sites. In our previous work,[75] the *in situ* growth of metallic MoS_2 on g-C_3N_4 nanosheets showed an even loading of MoS_2 nanolayers, while only random agglomeration could be formed *via* the *ex situ* mixing. Consequently, impressively enhanced activity for the photocatalytic synthesis of H_2O_2 was achieved *via* increased interfacial charge transfer, leading to a better performance in bacterial inactivation by the photogenerated germicide H_2O_2.

Moreover, flexible modification by various organic molecules[50,76,77] has been another strategy of great interest for the photocatalytic synthesis of H_2O_2 using g-C_3N_4. For example, Yang and coauthors[68] assembled perylene imide (PI) on rich inherent amine edges of g-C_3N_4 nanosheets to form a Z-scheme heterojunction. The photoexcited h^+ left on the VB of PI could oxidize water to $^{\bullet}OH$ and the following combination of two $^{\bullet}OH$ enabled the formation H_2O_2. Together with the $2e^-$ ORR pathway, this Z-scheme system resulted in two-channel photocatalytic H_2O_2 production (Fig. 5d), indicating the importance in band alignment design for semiconductor-based photocatalyst hybrids. Recently, the g-C_3N_4 photocatalyst was modified with cationic polyethylenimine (PEI) molecules by simply mixing in aqueous suspension due to their opposite surface charge.[78] The variation in local electronic environment was demonstrated by both DFT calculation and experimental characterization. The possible route for H_2O_2 formation was a sequential two-step $1e^-$ ORR based on the O_2-dependent performance and detection of $O_2^{\bullet-}$. The intermolecular electronic interaction in PEI/g-C_3N_4 together with intrinsically protonated PEI serving as a H^+ relay promoted both the activity and selectivity for the photocatalytic synthesis of H_2O_2. As mentioned above, AQ can selectively serve as an oxygen reduction site, and cobalt species can act as a water oxidation site for O_2 evolution. In a recent report, loading both of them as reductive and oxidative sites on C_3N_4 resulted in inhibited charge recombination for an enhanced H_2O_2 production rate and selectivity. A center/edge approach was proposed to separately load single-atom Co and AQ molecules based on the rational design of the fabrication procedure, such as homogeneous dispersion of Co precursor and rich amino groups at the edge of C_3N_4 to bind with carboxylic groups in the AQ precursor, instead of unregulated loading and distribution of two cocatalysts.[79]

In the electrocatalytic production of H_2O_2, an example of a g-C_3N_4-based gas diffusion electrode (GDE) was reported, where by covalently modifying with AQ, the generation rate of H_2O_2 increased by 20 times and 4 times, respectively, compared to that of the bare g-C_3N_4 GDE and AQ-g-C_3N_4 conventional immersed electrode.[80] g-C_3N_4 was proven to be an amiable substrate for chemically bonding AQ (20 wt%) as an electrocatalytic redox reaction center for H_2O_2 formation from $2e^-$-ORR, although the overpotential (900 mV) was relatively large for an optimal performance due to the weak conductivity of g-C_3N_4 and the maximum faradaic efficiency was only 42.2% (which could be caused by hydrogen evolution reaction (HER) on the g-C_3N_4 surface covered with AQ). Furthermore, combining g-C_3N_4 with a conventional electrode (activated carbon (AC) fiber) could drive the photoelectrochemical (PEC) production of H_2O_2 to directly degrade phenol.[81]

Reduced graphene oxide (rGO) is another well-known electron mediator for photoexcited charge separation on semiconductors.[50,82,83] Electronic interactions were found in some multiple-component photocatalyst systems based on g-C_3N_4, where rGO accepted photoexcited e^- from g-C_3N_4 and promoted the reductive production of H_2O_2 (inherent oxygen functional groups on rGO possibly being the active sites).

3.2. Graphene and its hybrids

3.2.1. Modification of graphene. Graphene is a single well-defined layer of sp^2-hybridized carbon. Its unique properties (such as high electronic conductivity and stability) and 2D structure make it a widely used catalyst or catalyst support, mostly in terms of graphene oxide (or rGO) and heteroatom-doped graphene, because pristine graphene is considered inert in catalysis.[84,85] Oxygen functional groups, defects, and doped elements are generally the active sites in reactions catalyzed by graphene-based materials, originating from the change in electrical state.[86]

Specifically, thermally reduced graphene oxide was studied as an electrocathode to catalyze oxygen reduction to H_2O_2.[34] The overpotential was as low as 10 mV and completely selective $2e^-$ ORR was realized, exceeding that of the state-of-the-art catalysts reported at that time (Fig. 6b). According to the FTIR spectra (Fig. 6a), the peak assigned to the ring ether groups at the sheet edge of 600 °C mrGO (mild reduction of graphene oxide) was much more obvious than that of the other samples. Combined with results of a series of spectroscopic analyses and *in situ* Raman spectroscopy (which has not been exploited before), the sp^2-hybridized carbon near-ring ether defects were identified as the active sites, while for F-mrGO (few-layered mrGO) the epoxy groups on the basal planes were the active sites (Fig. 6c). The likely overoxidation during the fabrication of graphene (typically by Hummers' method) induces abundant in-plane carbon lattice defects, which may improve the catalytic activity when the density of defects is appropriate or negatively influence the performance when the defects are excessive (one possible reason is the lower electrical conductivity).[87] This was explored by Han and coauthors using graphene/GO precursors with different defect densities in the electrochemical reaction for $2e^-$ ORR to H_2O_2.[88] After ammonium hydroxide treatment of the precursors to induce N doping, the highest selectivity was found with the lowest
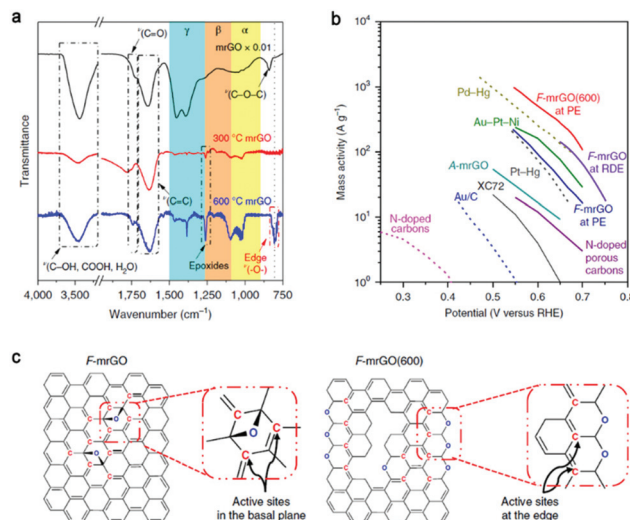
Fig. 6 (a) FTIR spectra of various mrGO powder samples. (b) Mass activity of different electrocatalysts for H_2O_2 production. The data presented as dashed lines was measured in acidic conditions (0.1 M $HClO_4$) and that as solid lines was measured in basic conditions (0.1 M KOH). (c) Idealized schemes of proposed low-overpotential active sites on F-mrGO and F-mrGO (600). Reproduced with permission.[34] Copyright 2018 Springer Nature.

defect density precursor, and the activity was optimized at 0.2 V (vs. RHE). This indicates that the content of in-plane carbon lattice defects should be controlled when designing carbon-based electrocatalysts for the production of H_2O_2.

Hydrogen peroxide is commonly used in advanced oxidation processes to degrade organic pollutants. Su and coauthors modified a graphite felt cathode with regulable N-doped graphene.[89] According to their investigation, graphite N was proven to favor the $2e^-$ reduction of O_2, while pyridinic N catalyzed H_2O_2 to produce $^{\cdot}OH$, which was the dominant oxidant for the following phenol degradation. Compared to conventional electro-Fenton system, the dependence on solution pH was greatly minimized in this electrochemical process.

Notably, bare graphene oxide, possessing a semiconducting band gap, was demonstrated to directly catalyze H_2O_2 production driven by simulated sunlight in the absence of an organic electron donor.[90] A higher production rate was achieved at a higher pH; however, more severe photocorrosion occurred because of the possible reduction of graphene oxide.

3.2.2. Hybridization strategy. Composite catalysts based on graphene are usually employed to improve the photocatalytic synthesis of H_2O_2, where photoabsorbers (e.g. TiO_2, carbon nitride, CdS and coordination polymers) are adopted to initiate the photoexcitation of charge carriers and rGO acts as an electron mediator and reduction active site.[91–94] In our previous work utilizing photogenerated ROS for water disinfection, the promoted formation of H_2O_2 was responsible for the generation of oxidative species on two different TiO_2 semiconductor-based ternary nanocomposites catalysts modified by rGO nanosheets.[95–97] Two distinct routes were observed for the formation of H_2O_2 by, specifically, the photoreduction of

O_2 via a $2e^-$ pathway on TiO_2/rGO/WO_3, where a Z-scheme system was constructed between TiO_2 and WO_3, and the recombination of $^{\cdot}OH$ on TiO_2/carbon dots/rGO, where carbon dots functioned further as an e^- acceptor, with charge carrier migration mediated by rGO in both routes. However, the adjustment of selectivity towards H_2O_2 was not a priority since a higher inactivation performance was the ultimate objective. Another ternary hybrid consisting of triplet–triplet annihilation (TTA) upconversion (UC) chromophore, CdS and graphene oxide nanodisks (GOND/CdS/TTA-UC) was established as a multi-functional photocatalyst for low energy photon excitation.[97] The photoresponse of the CdS semiconductor was extended from the wavelength of 505 nm to 635 nm via the TTA-UC effect, and e^- from CB of CdS was trapped by GOND, which acted as reductive sites for the $2e^-$ ORR. Consequently, light utilization, spatial charge separation and reduction in photocorrosion were realized simultaneously. This three-in-one heterostructure can obviously prove a design concept successful; however, it usually involves laborious synthetic steps, hampering its future commercial production, and its high complexity makes it a non-ideal model to identify active sites precisely.

Besides the commonly used graphene sheet, graphene quantum dots (GQD) with dual dopants (nitrogen and sulfur) were anchored on the surface of TiO_2 and the photocatalytic generation of H_2O_2 was superior to bare TiO_2 and TiO_2 modified with undoped GQD and N-doped GQD. According to the theoretical analyses, the authors suggested that N- and S-codoped GQD could offer active sites for the formation of *OOH and proton relays, thus promoting proton-coupled electron transfer for O_2 reduction to H_2O_2.[92] However, dual dopants are not always beneficial for the catalytic formation of H_2O_2. As is known, the $2e^-$ ORR was an undesirable reaction and needed to be suppressed for the selective ORR through a $4e^-$ pathway. The additional doping of boron or phosphorous on a N-doped graphene electrocatalyst facilitated the $4e^-$ ORR by minimizing H_2O_2 production because it enhanced the asymmetry of the spin density or electron transfer on the basal plane of the N-doped graphene and reduced the energy gap between the highest occupied molecular orbital (HOMO) and the lowest unoccupied molecular orbital (LUMO) of graphene.[98] In the case of the electrochemical formation of H_2O_2 from O_2 by graphene-based hybrids, Nb_2O_5/rGO sheets improved the H_2O_2 production in acidic media in contrast to the pristine rGO cathode, although the enhancement was not significant.[99] In an electro-Fenton system, when a traditional graphite-based gas diffusion cathode was integrated with rGO, it presented a better performance for the removal of organic dye (98% removal rate over 60 min) and a lower energy consumption.[100]

3.3. Nanostructured carbons beyond graphene

Carbon nanostructures, including nanodots, nanohorns, nanotubes, nanosized architectures and porous carbon with flexible structure engineering (Fig. 7) have been widely utilized in catalyzing the synthesis of H_2O_2.[7,32,101–108] They act as active cata-
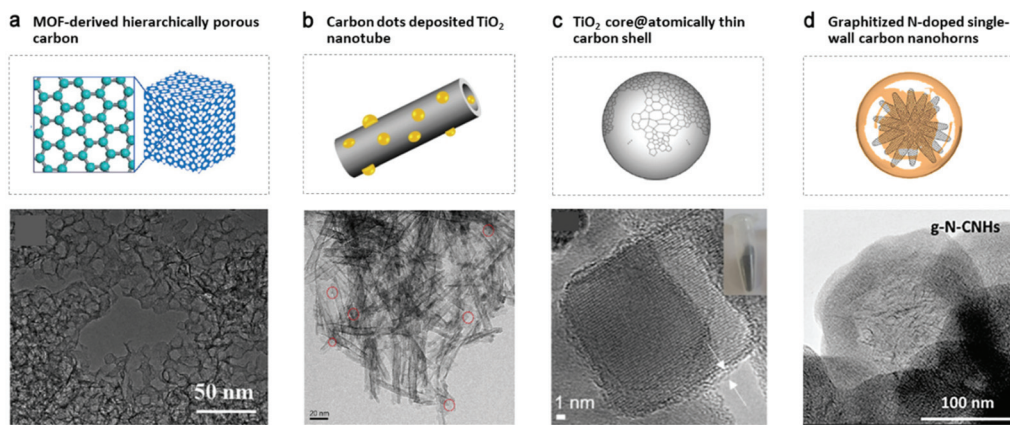
Fig. 7 Nanostructured carbon catalysts. (a) Metal–organic framework (MOF)-derived hierarchically porous carbon (fabricated *via* the hydrothermal growth of MOF following pyrolysis at 1100 °C under an H_2 atmosphere). Reproduced with permission.[108] Copyright 2015 WILEY-VCH Verlag GmbH & Co. KGaA, Weinheim. (b) Hybrids of TiO_2 nanotubes with carbon dots, obtained from P25 TiO_2 by NaOH, HNO_3 and citric acid treatment. Reproduced with permission.[103] Copyright 2019 Elsevier. (c) TiO_2 naoparticle@C core−shell structure (through pyrolytic decarboxylation of the adsorbed aromatic compounds). Reproduced with permission.[105] Copyright 2019 American Chemical Society. (d) Graphitized N-doped single-wall carbon nanohorns (g-N-CNHs), prepared *via* a multi-step protocol: oxidization of CNHs, combination with dopamine hydrochloride and polymerization, and thermal treatment at 700 °C under an argon atmosphere. Reproduced with permission.[102] Copyright 2018 Elsevier.

lysts, substrates (mostly to support metals or metal alloys nanoparticles due to their large surface area and high conductivity),[27] and photogenerated charge carrier mediators. They can be optimized in terms of heteroatom doping,[109–114] surface oxidization,[32,115] porous structure tuning,[108,116] and defect design[117] with in-depth studies aiming to reveal their structure-to-activity mechanisms. Some of the experimental results showed their comparable and even better performances relative to metal catalysts.[32,108]

3.3.1. Porous carbon. Porous carbon materials have gained increasing attention in electro- and photocatalysis because of their high surface area and pore volume, numerous defect sites and decent electronic conductivity.[118] They are among the most early-developed cathode materials, ranging from AC to heteroelement-doped porous carbon.[7] The different porous structures, such as mesoporous, microporous and hierarchically porous, show varying effects in catalytic performance for the formation of H_2O_2 (generally with good activity and selectivity).[117] However, when porous carbons are further tuned by modification such as heteroatom doping or oxidization, their activity and selectivity for oxygen reduction become more dependent on these foreign perturbations rather than their porosity.[119] A mechanistic study to identify the precise ORR active sites using a carbon-based model catalyst showed that pyridinic N created Lewis base sites and made the adjacent carbon atom adsorption site of oxygen molecule atoms in the initial step for oxygen reduction.[120] Nevertheless, the selective $2e^-$ ORR pathway was believed more encouraged with pyrrolic nitrogen-incorporated carbon, as supported by the observation that a higher selectivity for the electrosynthesis of H_2O_2 was obtained with the catalyst synthesized at a lower carbonization temperature and possessing a higher content of pyrrolic nitrogen.[101,121] The favored formation of H_2O_2 by pyrrolic N-doping was also observed in an electro-Fenton process for

the efficient degradation and mineralization of sulfathiazole.[122] Furthermore, the high electronic conductivity and stability resulted from N-doping potentially ensure better catalytic activity. On covalent organic framework-derived porous carbon, graphitic N was thought to be crucial for the $2e^-$ ORR.[109] In 2015, a more detailed correlation between porous structures and H_2O_2 production by electroreduction was first investigated on MOF-derived hierarchically porous carbon (Fig. 7a).[108] The order of the BET surface area and electrocatalytic activity ($2e^-$ ORR) followed the same trend over a series of samples, where the porous structures were tuned by the duration of hydrothermal reaction (to grow MOF template). Comparing the surface area-normalized current efficiency, a higher ratio of sp^3- to sp^2-bonded C and defects for catalyst carbonized under H_2 atmosphere was thought to be responsible for the higher selectivity and activity. Both the H_2O_2 production rate and current efficiency in acidic/neutral solution were reported to be among the highest. Accordingly, it will be of interest to graft this catalyst in a solar-driven H_2O_2 emission system, *e.g.* as a potential support for photoabsorders. Besides nitrogen as a popular dopant, fluorine doping also favored oxygen reduction to H_2O_2 by promoting the adsorption of O_2 and desorption of OOH.[113] Using an optimized F-doping configuration, the selectivity and production rate were elevated to 93.6% and 792.6 mmol h^{-1} g^{-1}, respectively.

3.3.2. Oxidized carbon. Surface oxidation treatment of carbon-based materials is an effective approach for improving their catalytic performance for the formation of H_2O_2.[123] In an earlier report in 2008, an AC cathode was used in an electrochemical setup with exposed solid polymer electrolyte, where continuous H_2O_2 production was observed and improved.[7] The authors hypothesized that the origin of the activity was the oxygen functional groups on the surface of AC, after the removal of which, H_2O_2 production ceased, while HNO_3 treat-

ment and oxidation both enhanced the performance of the AC catalyst. The surface chemistry of a boron-doped diamond (BDD) electrode was also studied for the cathodic formation of H_2O_2 *via* preanodization treatment.[115] Before the cathodic reaction, the anodic potential applied oxidized the sp^2 carbon on the boundary of the nanocrystalline diamond grains, and then influenced reductive H_2O_2 generation positively with an increase in current density. This approach relied on the repeated input of oxidative and reductive potentials instead of the static potential normally used. However, both of the above-mentioned works did not disclose the role of specific oxygen functional groups. A more detailed work in 2018[32] confirmed the positive correlation between surface oxygen functional groups and activity and selectivity of electrocatalytic 2e⁻ ORR H_2O_2 production on oxidized CNT, and the generality of their tailoring on other types of oxidized carbon (Fig. 8a–c). Among the various oxygen functional groups and configurations (Fig. 8d and e), the carbon atoms adjacent to C–O on the basal plane and COOH at the armchair edge (graphene was used as the model system) were identified to be the active sites with the limiting potential closest to equilibrium potential (*i.e.* lowest overpotential), which is comparable to reported precious metal catalysts (Pt–Hg and Pd–Au). The DFT calculation results explained the outstanding performance and were verified by further experimental evidence. Notably, the etheric group in this reported model and that in mildly reduced graphene oxide were both identified as active sites for electroreduction of O_2 towards H_2O_2 in basic and neutral electrolyte, which would be of interest to intentionally introduce etheric groups for further 2e⁻ ORR catalyst design under similar conditions.

3.3.3. Other nanostructured carbons. Carbon nanodots with a size of generally less than 10 nm are easily to be anchored on different substrates as cocatalysts. Carbon nanodots have been coupled with semiconductors, for instance TiO_2 (Fig. 7b for photocatalytic 2e⁻ ORR) and CoP (for photochemical water splitting into H_2 and H_2O_2 *via* a 4e⁻–2e⁻ cascaded pathway, Fig. 5f) to accept photoexcited electrons on the CB side and become reduction active sites.[103,124] Besides the catalytic activity of TiO_2 for the formation of H_2O_2, it can also catalyze the decomposition of H_2O_2 together with decomposition caused by ultraviolet range irradiation to excite excitons across a wide band gap. Enclosing the TiO_2 core with a carbon shell (Fig. 7c) can retard the consumption of the generated H_2O_2 and provide additional active reduction sites through pyrolytic decarboxylation of the adsorbed single molecular layer of aromatic compounds.[105]

The assembly of different low-cost carbon materials can potentially enhance their electrochemical performance. For example, Khataee *et al.* systematically compared the cathodic generation of H_2O_2 on a bare graphite electrode and modified ones (with immobilized AC and CNT).[125] Both AC and CNT were found to be beneficial in the electrogeneration of H_2O_2 with an improvement of 3- and 7-fold, respectively, compared to bare graphite. A suitable applied current, air flow rate, and acidic electrolyte formed optimized operating conditions. Amorphous carbon, as another important carbon electrode characterized by mixed sp^2/sp^3 carbon bonds, was examined in
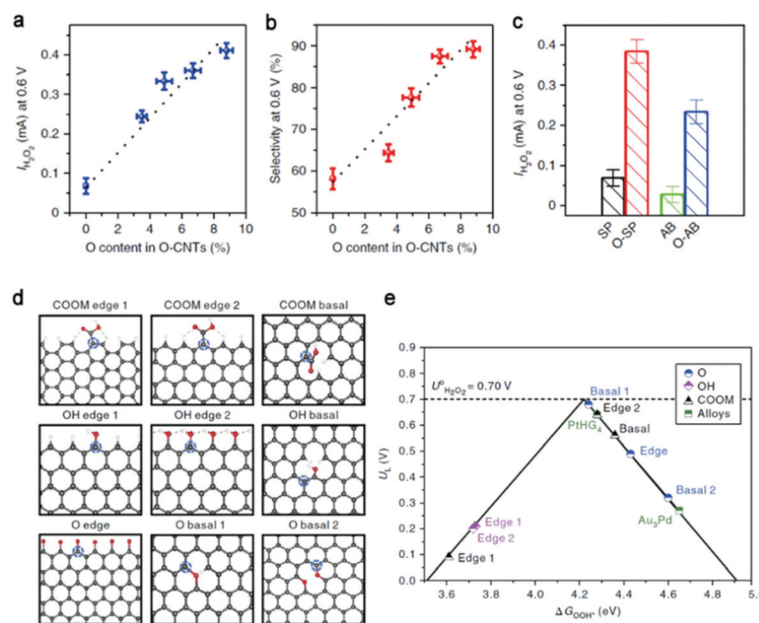

Fig. 8 Plots of H_2O_2 current (a) and selectivity (b) at 0.6 V as a function of oxygen content for O-CNTs with various oxidation times, demonstrating that both the activity and selectivity correlate linearly with the oxygen content. (c) H_2O_2 current (0.6 V) comparison of SP, O-SP, AB and O-AB, suggesting that the oxidation process is generally applicable for carbon materials. (d) Different oxygen functional group type configurations. The carbon atoms denoted by a blue circle are the active sites under investigation (M = H and Na). (e) Calculated two-electron (solid black) ORR-related volcano plot for the electro-reduction of oxygen to H_2O_2 displayed with the limiting potential plotted as a function of ΔG_{OOH*}. The equilibrium potential for the two-electron ORR is shown as the dashed black line. Reproduced with permission.[32] Copyright 2018 Springer Nature.

terms of correlation between sp^2 carbon content and capability of producing H_2O_2 with varying percentages of sp^2 C bond over a wide range by tuning the fabrication parameters.[126] The maximum H_2O_2 production was afforded by the highest content of sp^2 C bond. A very impressive overall performance for the electroreduction of O_2 to H_2O_2 was achieved.[102] A metal-free catalyst system was prepared, which possessed a unique carbon nanohorn core, suitable porosity, and a profitable distribution of two types of doped N sites (Fig. 7d). The catalyst system worked well under acidic, physiological and alkaline conditions (pH = 1, 7.4 and 13, respectively) with a faradaic efficiency up to 98% and relatively low overpotential.

3.4. Emerging organic catalysts

Using organic materials with abundant feedstocks as catalysts can offer sustainable and affordable regulation of reactions in terms of environment remediation and energy generation, especially when solar light can solely drive the catalytic reaction in the case of organic semiconductors.[127,128] They often show flexibility in tuning their chemical and electronic structure. Some exciting achievements have been presented recently.

The stability of organic catalysts themselves against photo-corrosion is a precondition. Głowacki's group[129,130] developed several highly stable organic systems for the photo(electro)catalytic reduction of oxygen to H_2O_2 in a wide range of pH (roughly 1–12), i.e. H-bonded pigments (Fig. 9a) and biscou-
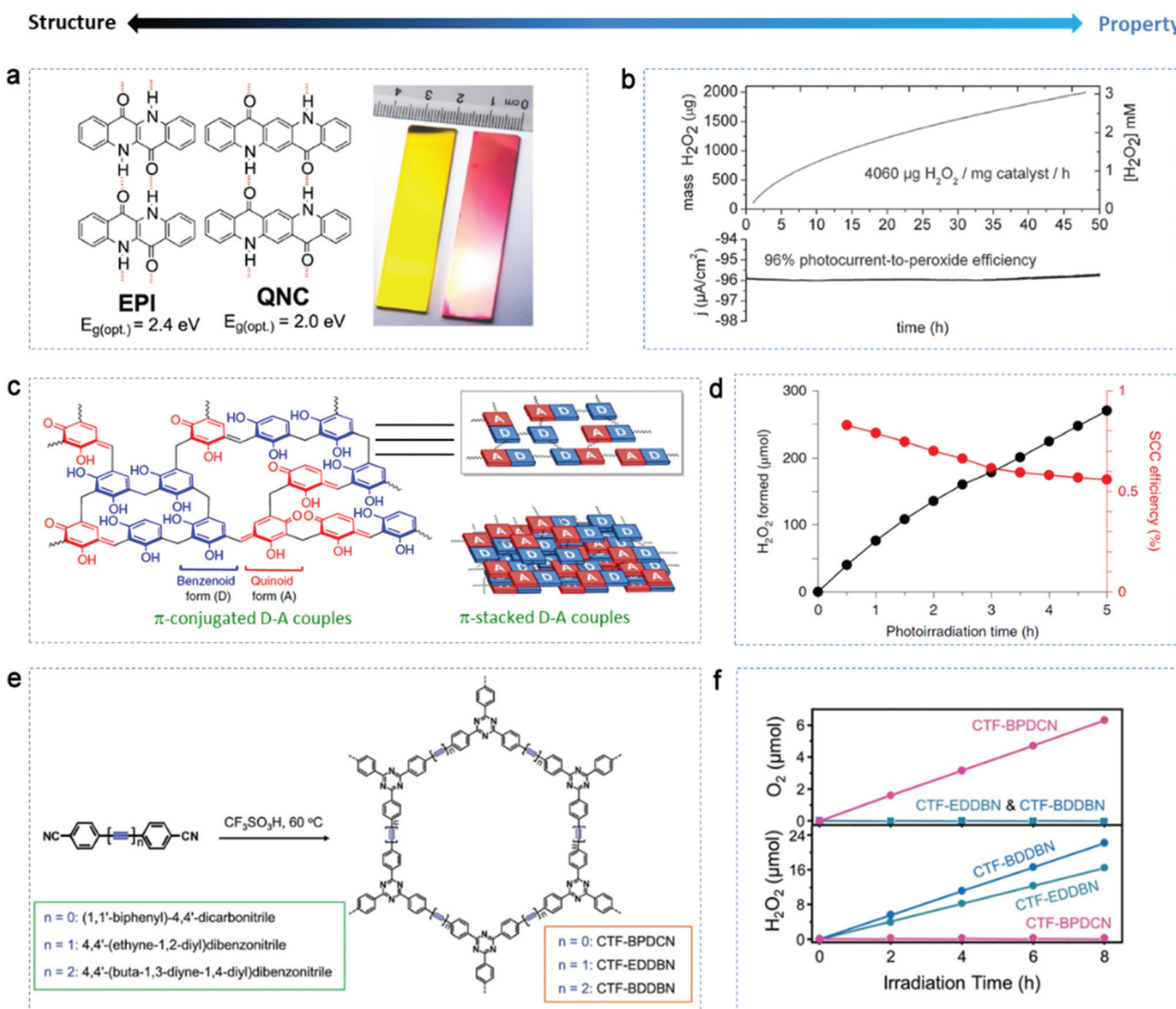
Fig. 9 Organic semiconductors for photo(electro)catalytic H_2O_2 production. (a) Hydrogen-bonded pigment semiconductor epindolidione (EPI) and quinacridone (QNC) and a digital picture of EPI (yellow) and QNC (red) photoelectrodes. (b) Photocathodic H_2O_2 evolution in a two-compartment cell with EPI on a Cr/Au working electrode. Reproduced with permission.[129] Copyright 2019 WILEY-VCH Verlag GmbH & Co. KGaA, Weinheim. (c) Fundamental structure and π-conjugated and π-stacked D–A structure of RF resins. (d) Changes in the amounts of H_2O_2 generated on RF523 and SCC efficiency. Adapted with permission.[37] Copyright 2019 Springer Nature. (e) Scheme of the synthesis of covalent triazine frameworks (CTF) from their corresponding precursors. (f) Time-dependent formation of H_2O_2 or O_2 by WOR with different CTF. Reproduced with permission.[131] Copyright 2019 WILEY-VCH Verlag GmbH & Co. KGaA, Weinheim.

marin-containing acenes, with no detectable self-degradation. Notably, these organic catalysts were able to produce H_2O_2 in the absence of sacrificial alcohol and the catalyst dosage-normalized H_2O_2 yield was as high as 4060 mg g^{-1} h^{-1} (Fig. 9b), exceeding the pioneering results on g-C_3N_4 (0.7 mg g^{-1} h^{-1}). However, the concentration accumulated was only 3 mM. The mechanism was proposed to be similar to that of the quinone/hydroquinone system, where the organic molecules act as reaction carriers, following the steps of: (i) photoexcitation of molecules from the ground state, (ii) protonation and photoreduction of the excited basic carbonyl groups resulting in a reduce *enal* state, (iii) nucleophilic attack on dissolved O_2 and formation of a tetrahedral intermediate, and (iv) dissociation of the intermediate releasing HO_2^-, which abstracts a proton from another *enol* unit, thus regenerating the ground-state molecule and yielding one H_2O_2 molecule.

Very recently, Shiraishi's group[37] presented crosslinked polymer semiconductors, resorcinol-formaldehyde (RF) resins (Fig. 9c), increasing the efficiency of artificial photosynthesis (not only H_2O_2 production) on powder catalysts towards an unprecedentedly high level (above 0.5% solar-to-chemical conversion efficiency). The increase in temperature during hydrothermal reaction for the fabrication of the RF resins had a positive influence on their catalytic activity, with the resin obtained at 523 K generating the maximum H_2O_2 of 62 μmol in 24 h. A relatively stable and high SCC was reached when increasing the catalyst dosage and photoreaction temperature (Fig. 9d), even though self-oxidation of the resins was observed in the initial stage, which is quite common with organic catalysts. The authors conducted a detailed investigation on the relation between resin structure and optical/electronic properties. Briefly, the methylene-crosslinked π-conjugated quinoid (electron acceptor)-benzenoid (electron donor) resorcinol chains formed a low HOMO–LUMO gap and the graphitic π-stacked chains led to a hybridized HOMO–LUMO level and low bandgap (2.0 eV, active with 700 nm photons). The suitable band structure of the RF resins enabled the photoreduction of O_2 to H_2O_2 in pure water ($2H_2O + O_2 \rightarrow H_2O_2$). Hence, this inexpensive and efficient metal-free semiconductor with one-pot synthesis and wide light-response is particularly promising for the photosynthesis of H_2O_2.

In comparison to the dominant $2e^-$ ORR (or a sequential two-step $1e^-$ ORR), water oxidation towards H_2O_2 has not yet been well investigated and optimized on carbon-based catalysts; however, it has a higher atom utilization efficiency. Accordingly, Xu's group[131] managed reaction the pathway for the photosynthesis of H_2O_2 based on the control of the chemical structure of covalent triazine frameworks (CTF) with the modification of acetylene (–C≡C–) and diacetylene (–C≡C–C≡C–) moieties (Fig. 9e). The functionalized CTF generated H_2O_2 by both oxygen reduction and water oxidation *via* a two-electron process (pathway is shown in Fig. 5e), while only the former occurred on the C–C triple-bond-free CTF (Fig. 9f). ΔG_{OH*} was used as a descriptor to analyze whether or not the formation of OH* intermediate is thermodynamically favored compared to the formation of ˙OH radical ($\Delta G_{˙OH}$). When

acetylene or diacetylene was the active site, ΔG_{OH*} was much lower, which explained the novel $2e^-$ WOR on the C≡C functionalized CTF, where charge separation was also encouraged.

Nevertheless, photocatalysis by organic materials is still in its infancy, and thus attempted trials would be encouraged even with unsatisfactory experimental findings at present. A mass-produced biopolymer, lignin, was examined for the photochemical generation of H_2O_2.[132] Lignin underwent autooxidation, *i.e.* degradation, simultaneously with reductive H_2O_2 formation. The oxidation of oxalate, the added electron donor, competed with that of lignin and the redox reaction in total was increased simultaneously, reaching a maximum turnover number (TON) of 17 254 μmol g^{-1}. Although, lignin failed to be a valid photocatalyst, the green H_2O_2 production upon the degradation of lignin or the byproducts of photooxidation can be potentially of interest in some applications.

The control of both the composition and microstructure of catalysts at the molecular level is essential for disclosing the mechanism of reactions. Thus, for the study of the electrochemical production of H_2O_2 and to gain theoretical insight, Briega-Martos *et al.*[133] selected an aza-fused π-conjugated microporous polymer (Aza-CMP, Fig. 10a), which was assembled from molecular building blocks, with rich pyridinic N as the single dopant. Aza-CMP presented a high H_2O_2 selectivity under a tiny overpotential, while post-treatment with Co(II) catalyzed the further reduction of H_2O_2 to H_2O (Fig. 10b). The DFT results indicated that the hydrogenation of pyridinic N could destabilize neighboring carbon atoms slightly, which became the adsorption sites for O_2 to form superoxide species (from the partial Mulliken charges in Fig. 10d) in a monodentate chemisorbed state (Fig. 10c). The chemisorbed state resulted in the less stable adsorption of oxygen molecules compared to physisorbed state, which restrained the breaking of the O–O bond, leading to the partial reduction of O_2 to H_2O_2. Although the activity of this system was not high, it provided insight into the ORR mechanism on polymer catalysts.

Despite the intriguing advantages of the light-driven production of H_2O_2, its efficiency is still far from satisfactory since the separation and migration of photogenerated charge carriers lack a driving force. PEC cells can induce spatial charge separation. Thus, a metal-free polyterthiophene (pTTh) coating was used as photocathode for oxygen reduction to H_2O_2, and a record high H_2O_2 concentration of 110 mM was accumulated in alkaline electrolyte (pH ∼ 13).[134] When combined with the NiFeO$_x$/BiVO$_4$ photoanode as an O_2 evolution catalyst, the authors constructed a bias-free system (Fig. 11a), which retained outstanding activity and stability. The $2e^-$ and $4e^-$ pathways were accompanied with the key steps of C-OOH and CO-OH cleavage, respectively (Fig. 11b). According to the calculation results, C-OOH cleavage to release peroxide ion HO_2^- ($S_3 \rightarrow S_0$) was favored by a relatively lower energy and this reaction rate was ∼218 times faster than the rate for hydroxide ion formation ($S_3 \rightarrow S_4$) *via* CO-OH cleavage. The energy profile was affected by pH, with a lower pH value to facilitate the $4e^-$ process, making the pH a sensitive regulator.
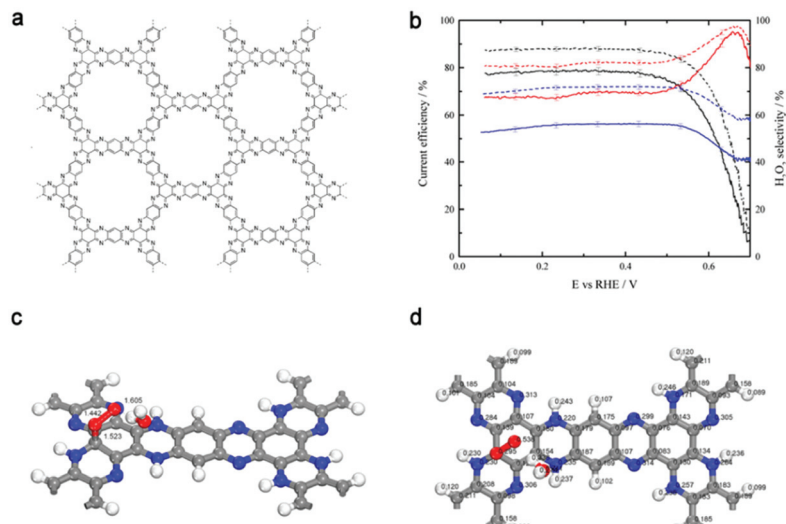
Fig. 10 (a) Structure of the aza-fused π-conjugated microporous polymer (Aza-CMP). (b) Current efficiency (solid lines) and H_2O_2 selectivity (dashed lines) for the ORR reaction on the Aza-CMP (red line), Aza-CMP@Co (blue line), and glassy-carbon (black line) electrodes in O_2-saturated 0.1 M NaOH solution. (c and d) Monodentate chemisorbed state of molecular oxygen on the carbon atom. (c) Adsorbent-adsorbate-solvent geometry (lengths given in Å). (d) Mulliken partial charges (e). Explicit water molecule in addition to a continuum model was used as a solvation effect treatment. Reproduced with permission.[133] Copyright 2017 American Chemical Society.
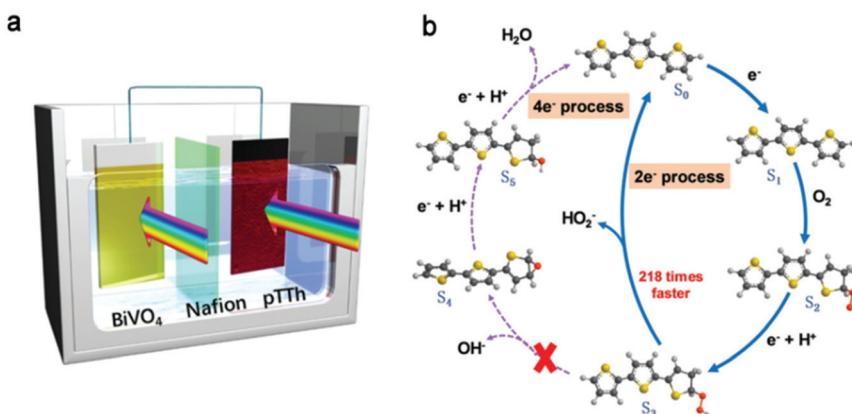
Fig. 11 (a) Illustration of the unbiased H_2O_2 production device, with pTTh as the photocathode and $NiFeO_x/BiVO_4$ as the photoanode in 0.1 M KOH and 1 M borate buffer electrolyte, respectively. (b) Proposed reaction cycles of H_2O_2 production with the energetically most feasible active sites. S_0 is the bare surface and S_x (x = 1, 2, 3, 4, and 5) are the structures of the intermediate states involved in the ORR. Red, gray, yellow and black balls represent oxygen, hydrogen, sulphur and carbon, respectively. Reproduced with permission.[134] Copyright 2020 Royal Society of Chemistry.

4. Highlighted carbon-based materials for 2e⁻ or 4e⁻ ORR

To maximize the energy capacity, the 4e⁻ ORR is a desirable reaction in fuel cells and metal-batteries.[135,136] Extensive studies have been carried out to develop carbon-based catalysts, which are abundant in nature, to replace platinum catalysts for the 4e⁻ reduction. However, the exact origin and structure of the ORR active sites remain unclear. Here, we present some important experimental and theoretical highlights on carbon platforms. For the 4e⁻ ORR, carbon nanostructures doped with nitrogen, such as N-doped CNT and graphene, have shown similar activity and superior stability and dura-

bility to commercial Pt/C catalysts, especially in alkaline electrolyte.[137–139] Among the configurations of nitrogen species, pyridinic and pyrrolic nitrogen atoms are mostly likely to facilitate the 4e⁻ ORR process, while their counterparts without N doping preferably form H_2O_2 first (substantially go reduction or oxidation, but usually the direct 4e⁻ route affords higher complete ORR activity and thus is more desirable). The electron-accepting nitrogen induces charge delocalization, which can make adjacent carbon atoms positively charged, to affect the adsorption of O_2 and breakage of O–O bond and to function as oxygen reduction active sites. This hypothesis was further evidenced in a recent report using graphite model catalysts with N-doping more precisely controlled.[120] The role of

pyridinic N was emphasized again. Sometimes, metal and nitrogen coordinations are thought to be the exact reduction sites. However, each conclusion is largely dependent on synthesis of the catalyst materials. High temperature annealing of carbon materials under N-rich atmosphere (*e.g.* ammonia) or using N-containing precursors often results in active N-sites, while N doping realized by hydrothermal reaction (150 °C, with NH_4OH) does not demonstrate a similar trend (reduced electron number was calculated to be ~2.7).[140] Instead, it was found to facilitate the anchoring of the active metal sites. Moreover, even with a similar doping method, active nitrogen could be doped as quaternary type rather than pyridinic or pyrrolic N.[135] Other factors such as geometry (alignment or roughness of carbons) are less related to the electrochemical mechanism for the ORR, but relevant to the electrokinetics. For the $2e^-$ ORR, N-doping was also repeatedly reported beneficial to form H_2O_2 selectively (particularly for oxygen electroreduction), mostly using mesoporous carbon materials.[101,112,114] However, clear mechanisms have not been reported to date. We speculate that the high exposure of surface/edges in these porous structures may affect the doping position of nitrogen and alter the way that the N sites regulate the ORR mechanism. In addition, doping with phosphorus and halogen atoms result in an enhancement in solar-driven H_2O_2 production.

On the other hand, many cases related the oxygen-containing functional groups on carbon catalysts (*e.g.* g-C_3N_4, rGO, CNT, AC and BDD) with active and selective $2e^-$ oxygen reduction, as discussed in the above.[7,32,34,54,115] The oxidization methods vary. In oxidized carbon nitride, according to the theoretical energy evolution for each reaction step, C–O–C was much more favorable in energy than that of other functional groups. In oxidized graphene, the configurations of oxygen groups have an obvious influence on activity towards H_2O_2 (as a function of ΔG_{OOH^*}, Fig. 8d and e, scaling linearly with ΔG_{OH^*}, *i.e.* $\Delta G_{OOH^*} = \Delta G_{OH^*} + 3.2 \pm 0.2$ eV). The characterization evidence provided by Kim *et al.* to support the oxygen defect and property relationship was relatively solid. Just as they suggested, the etheric group should be eliminated when designing $4e^-$ ORR carbon catalysts. In other words, etheric group can be intentionally introduced for further developing high quality $2e^-$ ORR catalysts.

In theoretical studies, both activity and selectivity could be examined using ΔG_{OH^*} as a descriptor (Fig. 3). The catalysts with ΔG_{OH^*} close to the top of the $2e^-$ ORR volcano plots can potentially catalyze the reaction selectively and actively, which is also applicable as well for water oxidation towards H_2O_2. Tremendous efforts have led us to a deeper understanding of the ORR mechanism; however, new insights are still needed with characteristic evidence of catalysts and direct monitoring of the reaction intermediates.

5. Conclusions and perspectives

The last few years have witnessed fast development in the electro- and photocatalytic synthesis of H_2O_2 from water and oxygen in the aspects of engineering catalyst materials, optimizing operating conditions and designing reaction setups. Some inexpensive carbon-based catalysts show comparable (or even exceeding) electrochemical activity and selectivity to their noble metal counterparts. For example, the superior performance of oxidized carbon under alkaline conditions may allow the direct use of bulk solution in applications such as paper bleaching and the treatment of acidic wastewater.[32,34,141] The performance of carbon-based photocatalysts has also improved significantly in pure water systems, where electron/proton donors are no long necessary. Considering these advances, we may expect a massive reduction in capital input when these technologies are put into large-scale use with efficient, selective and cheap carbon-based catalysts, simultaneously being sustainable. However, some challenges are concluded here as suggestions for problems further works may deal with firstly.

Common problems for both electro- and photocatalytic systems are impurity of the bulk solution (other than water) and the self-degradation of catalysts. Generally, H_2O_2 solutions are desirable with moderate pH, and thus additional electron or hole scavengers and strong acidic or alkaline electrolytes should be avoided for most end users. During the redox reaction to form H_2O_2, catalysts themselves are likely to be oxidized or reduced when charge carriers accumulate on their surface for both anodic/cathodic electrodes and photoexcited semiconductors. Therefore, the intrinsic properties of materials against certain overpotentials or photocorrosion are important to be considered, and this importance becomes more significant in long-term operation. For example, WOR cocatalysts for H_2O to O_2 may relieve the photooxidation of carbonaceous $2e^-$ ORR photocatalysts by transferring h^+ to the active oxidation sites on the cocatalyst.

Another big challenge is to increase the H_2O_2 yield, which has been limited to several millimoles per litre per hour for most reported systems despite the modification of catalysts (with a very few exceptional yields of 89–116 mM h^{-1} in electrochemical synthesis).[32,108] As is known, some materials originally reported as photocatalysts have been later employed as electrocatalysts (such as g-C_3N_4),[45] and *vice versa* (such as WO_3 and $BiVO_4$).[28] The major difference between them is that photoabsorbers are requisite in a light-driven process. Thus, expended light response to the visible range should be valued to mitigate H_2O_2 decomposition in the ultraviolet range. Higher conductivity is another critical factor to increase the charge transfer in both processes while in photocatalysis the separation of photoexcited e^-/h^+ pairs must be intentionally guided to withstand their fast recombination. However, there are several reports showing exciting performances by carbon-based materials. Porous carbon achieved H_2O_2 yield of 222.6 mM from electrosynthesis,[108] while only <30 mM could be used in sewage treatment and disinfection. A PEC system with a polymer photocathode produced 110 mM H_2O_2, which could be directly used in certain applications (for example, pulp and paper bleaching or H_2O_2 fuel cell for the generation of electricity).[134] Although other photocatalytic systems yielded less concentrated H_2O_2, they were capable of *in situ* fading
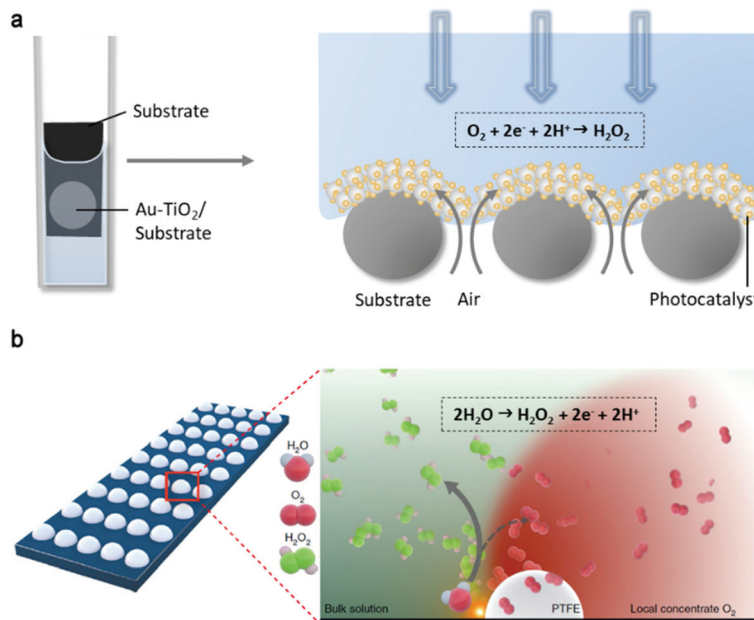
Fig. 12 (a) Schematic illustration of the triphase photocatalytic O_2 to H_2O_2 reaction system with Au-decorated TiO_2 photocatalysts immobilized on the porous superhydrophobic carbon fibers. Adapted with permission.[148] Copyright 2019 Elsevier. (b) Schematic showing the assumed possible reaction pathway of H_2O to H_2O_2 tuning by local confined oxygen on glassy carbon after hydrophobic treatment. Reproduced with permission.[142] Copyright 2020 Springer Nature.

dyes and killing bacteria.[75,100] Instead of predicted practical applications, a remarkable case was demonstrated that 50 ppm red basic Fuchsin dye in flowing water could be instantly degraded by continuously produced H_2O_2 solution (24 μmol min^{-1}) from water oxidation.[142] To fulfill wider and higher demands, an accumulation of >570 mM H_2O_2 (~2 wt%)[143] is desired by upgrading the state-of-the-art generation rate by several folds in the following development.

All the above properties (optical, electronic and physico-chemical) are related to the structure of materials, which also define the origin of selectivity and activity towards H_2O_2 formation. Nevertheless, some of the mechanical explanations remain rather speculative, especially when catalyst systems are prepared elaborately.[144,145] More direct experimental and simulated evidence is fundamentally needed based on the precisely controlled catalyst structures/components for in-depth understanding of their structure-to-property correlation, which is essential for the rational design of future catalysts. For instance, the bottom-up wet chemical approach could be employed for the more controllable synthesis of catalyst materials.[146] To gain insight, a combination of theory, computational studies, and sophisticated in situ/in operando characterization techniques will be beneficial.[147] Accordingly, researchers on heterogeneous catalysis can learn from each other to inspire ideas.

Besides the catalyst, the reaction can be boosted by designing the system setup. Since the reduction of oxygen to H_2O_2 involves the interaction among the catalyst, O_2 and liquid source of H$^+$ (photon incident also matters in photocatalysis), the reaction is supposed to be faster if one can facilitate their interaction.[149] Recently, an air–liquid–solid triphase photo-

catalytic architecture was reported to verify this concept (Fig. 12a).[148] O_2 from air was able to directly diffuse from the backside of the superhydrophobic (aerophilic) carbon fiber substrate to the front deposited Au-TiO_2 photocatalysts in a tri-phase system and the production rate was 44 times that of its liquid–solid diphase counterpart. Notably, the diffusion coefficient of O_2 in air (2.0×10^{-1} cm^2 s^{-1}) is about four orders of magnitude higher than that in H_2O (2.1×10^{-5} cm^2 s^{-1}). However, the H_2O_2 concentration increased slowly since decomposition was found to be dominant over generation. Thus, a subsequent separation step may solve this issue.[150] An interfacial engineering method was also demonstrated for anodic H_2O_2 generation on carbon electrodes (glassy carbon, Fig. 12b, and porous carbon fiber paper).[142] Hydrophobic polymers deposited on carbon electrodes locally confined O_2 (from 4e$^-$ WOR), thus shifting ΔG_{OH*} to the peak of the volcano, and consequently improving the activity and selectivity of the 2e$^-$ WOR to H_2O_2. Finally, authors combined this anode to oxidized CNT cathode in a flow cell for the 2e$^-$ WOR/2e$^-$ ORR strategy to directly fade organic contamination continuously. In the future, our reasonable yet ambitious anticipation is that electro- and photochemical H_2O_2 synthesis systems will be moving towards more active, selective and stable carbon-based catalysts, with affordable raw materials and feasible devices to open up opportunities in wide practical applications.

Conflicts of interest

There are no conflicts to declare.

Acknowledgements

References

1 R. Ciriminna, L. Albanese, F. Meneguzzo and M. Pagliaro, *ChemSusChem*, 2016, **9**, 3374–3381.

2 C. W. Jones, *Applications of hydrogen peroxide and derivatives*, Royal Society of Chemistry, 2007.

3 R. Hage and A. Lienke, *Angew. Chem., Int. Ed.*, 2006, **45**, 206–222.

4 R. A. Rozendal, E. Leone, J. Keller and K. Rabaey, *Electrochem. Commun.*, 2009, **11**, 1752–1755.

5 M. Melchionna, P. Fornasiero and M. Prato, *Adv. Mater.*, 2019, **31**, 1802920.

6 K. Kosaka, H. Yamada, K. Shishida, S. Echigo, R. A. Minear, H. Tsuno and S. Matsui, *Water Res.*, 2001, **35**, 3587–3594.

7 I. Yamanaka and T. Murayama, *Angew. Chem., Int. Ed.*, 2008, **47**, 1900–1902.

8 P. Drogui, S. Elmaleh, M. Rumeau, C. Bernard and A. Rambaud, *J. Appl. Electrochem.*, 2001, **31**, 877–882.

9 R. Pedahzur, H. I. Shuval and S. Ulitzur, *Water Sci. Technol.*, 1997, **35**, 87–93.

10 C. A. Martínez-Huitle and S. Ferro, *Chem. Soc. Rev.*, 2006, **35**, 1324–1340.

11 M. Ksibi, *Chem. Eng. J.*, 2006, **119**, 161–165.

12 I. V. Kozhevnikov, *Chem. Rev.*, 1998, **98**, 171–198.

13 G. Strukul, *Catalytic oxidations with hydrogen peroxide as oxidant*, Springer Science & Business Media, Netherlands, 2013.

14 Z. Jin, L. Wang, E. Zuidema, K. Mondal, M. Zhang, J. Zhang, C. Wang, X. Meng, H. Yang and C. Mesters, *Science*, 2020, **367**, 193–197.

15 K. Sato, M. Aoki, M. Ogawa, T. Hashimoto and R. Noyori, *J. Org. Chem.*, 1996, **61**, 8310–8311.

16 A. Sanli and A. Aytaç, *Int. J. Hydrogen Energy*, 2011, **36**, 869–875.

17 S. A. Mousavi Shaegh, N.-T. Nguyen, S. M. Mousavi Ehteshami and S. H. Chan, *Energy Environ. Sci.*, 2012, **5**, 8225–8228.

18 D. N. Prater and J. J. Rusek, *Appl. Energy*, 2003, **74**, 135–140.

19 J. M. Campos-Martin, G. Blanco-Brieva and J. L. Fierro, *Angew. Chem., Int. Ed.*, 2006, **45**, 6962–6984.

20 C. Xia, Y. Xia, P. Zhu, L. Fan and H. Wang, *Science*, 2019, **366**, 226–231.

21 J. K. Edwards, S. J. Freakley, R. J. Lewis, J. C. Pritchard and G. J. Hutchings, *Catal. Today*, 2015, **248**, 3–9.

22 S. Yang, A. Verdaguer-Casadevall, L. Arnarson, L. Silvioli, V. Čolić, R. Frydendal, J. Rossmeisl, I. Chorkendorff and I. E. Stephens, *ACS Catal.*, 2018, **8**, 4064–4081.

23 M. N. Young, M. J. Links, S. C. Popat, B. E. Rittmann and C. I. Torres, *ChemSusChem*, 2016, **9**, 3345–3352.

24 M. G. Clerici and P. Ingallina, *Catal. Today*, 1998, **41**, 351–364.

25 J. García-Serna, T. Moreno, P. Biasi, M. J. Cocero, J.-P. Mikkola and T. O. Salmi, *Green Chem.*, 2014, **16**, 2320–2343.

26 J. S. Hargreaves, Y.-M. Chung, W.-S. Ahn, T. Hisatomi, K. Domen, M. C. Kung and H. H. Kung, *Appl. Catal., A*, 2020, 117419.

27 Y. Jiang, P. Ni, C. Chen, Y. Lu, P. Yang, B. Kong, A. Fisher and X. Wang, *Adv. Energy Mater.*, 2018, **8**, 1801909.

28 S. C. Perry, D. Pangotra, L. Vieira, L.-I. Csepei, V. Sieber, L. Wang, C. P. de León and F. C. Walsh, *Nat. Rev. Chem.*, 2019, **3**, 442–458.

29 S. Fukuzumi, Y. M. Lee and W. Nam, *Chem. – Eur. J.*, 2018, **24**, 5016–5031.

30 H. Hou, X. Zeng and X. Zhang, *Angew. Chem., Int. Ed.*, 2019, DOI: 10.1002/anie.201911609.

31 A. Verdaguer-Casadevall, D. Deiana, M. Karamad, S. Siahrostami, P. Malacrida, T. W. Hansen, J. Rossmeisl, I. Chorkendorff and I. E. Stephens, *Nano Lett.*, 2014, **14**, 1603–1608.

32 Z. Lu, G. Chen, S. Siahrostami, Z. Chen, K. Liu, J. Xie, L. Liao, T. Wu, D. Lin, Y. Liu, T. F. Jaramillo, J. K. Nørskov and Y. Cui, *Nat. Catal.*, 2018, **1**, 156–162.

33 S. Siahrostami, A. Verdaguer-Casadevall, M. Karamad, D. Deiana, P. Malacrida, B. Wickman, M. Escudero-Escribano, E. A. Paoli, R. Frydendal, T. W. Hansen, I. Chorkendorff, I. E. L. Stephens and J. Rossmeisl, *Nat. Mater.*, 2013, **12**, 1137–1143.

34 H. W. Kim, M. B. Ross, N. Kornienko, L. Zhang, J. Guo, P. Yang and B. D. McCloskey, *Nat. Catal.*, 2018, **1**, 282–290.

35 M. Teranishi, S.-I. Naya and H. Tada, *J. Am. Chem. Soc.*, 2010, **132**, 7850–7851.

36 Z. Haider, H.-I. Cho, G.-H. Moon and H.-I. Kim, *Catal. Today*, 2019, **335**, 55–64.

37 Y. Shiraishi, T. Takii, T. Hagi, S. Mori, Y. Kofuji, Y. Kitagawa, S. Tanaka, S. Ichikawa and T. Hirai, *Nat. Mater.*, 2019, **18**, 985–993.

38 Y. Shiraishi, S. Kanazawa, Y. Sugano, D. Tsukamoto, H. Sakamoto, S. Ichikawa and T. Hirai, *ACS Catal.*, 2014, **4**, 774–780.

39 S. Siahrostami, G.-L. Li, V. Viswanathan and J. K. Nørskov, *J. Phys. Chem. Lett.*, 2017, **8**, 1157–1160.

40 B. O. Burek, D. W. Bahnemann and J. Z. Bloh, *ACS Catal.*, 2019, **9**, 25–37.

41 X. Shi, S. Siahrostami, G.-L. Li, Y. Zhang, P. Chakthranont, F. Studt, T. F. Jaramillo, X. Zheng and J. K. Nørskov, *Nat. Commun.*, 2017, **8**, 701.

42 A. Thomas, A. Fischer, F. Goettmann, M. Antonietti, J.-O. Müller, R. Schlögl and J. M. Carlsson, *J. Mater. Chem.*, 2008, **18**, 4893–4908.

43 F. K. Kessler, Y. Zheng, D. Schwarz, C. Merschjann, W. Schnick, X. Wang and M. J. Bojdys, *Nat. Rev. Mater.*, 2017, **2**, 1–17.

44 W.-J. Ong, L.-L. Tan, Y. H. Ng, S.-T. Yong and S.-P. Chai, *Chem. Rev.*, 2016, **116**, 7159–7329.

45 X. Wang, K. Maeda, A. Thomas, K. Takanabe, G. Xin, J. M. Carlsson, K. Domen and M. Antonietti, *Nat. Mater.*, 2009, **8**, 76–80.

46 D. Deng, K. Novoselov, Q. Fu, N. Zheng, Z. Tian and X. Bao, *Nat. Nanotechnol.*, 2016, **11**, 218.

47 T. Y. Ma, S. Dai, M. Jaroniec and S. Z. Qiao, *Angew. Chem., Int. Ed.*, 2014, **53**, 7281–7285.

48 Y. Hou, Z. Wen, S. Cui, X. Guo and J. Chen, *Adv. Mater.*, 2013, **25**, 6291–6297.

49 Y. Shiraishi, S. Kanazawa, Y. Kofuji, H. Sakamoto, S. Ichikawa, S. Tanaka and T. Hirai, *Angew. Chem., Int. Ed.*, 2014, **53**, 13454–13459.

50 Y. Kofuji, Y. Isobe, Y. Shiraishi, H. Sakamoto, S. Tanaka, S. Ichikawa and T. Hirai, *J. Am. Chem. Soc.*, 2016, **138**, 10019–10025.

51 G. Liu, P. Niu, C. Sun, S. C. Smith, Z. Chen, G. Q. Lu and H.-M. Cheng, *J. Am. Chem. Soc.*, 2010, **132**, 11642–11648.

52 Z. Zhu, H. Pan, M. Murugananthan, J. Gong and Y. Zhang, *Appl. Catal., B*, 2018, **232**, 19–25.

53 Z. Teng, W. Cai, S. Liu, C. Wang, Q. Zhang, S. Chenliang and T. Ohno, *Appl. Catal., B*, 2020, **271**, 118917.

54 Z. Wei, M. Liu, Z. Zhang, W. Yao, H. Tan and Y. Zhu, *Energy Environ. Sci.*, 2018, **11**, 2581–2589.

55 S. Li, G. Dong, R. Hailili, L. Yang, Y. Li, F. Wang, Y. Zeng and C. Wang, *Appl. Catal., B*, 2016, **190**, 26–35.

56 R. Wang, X. Zhang, F. Li, D. Cao, M. Pu, D. Han, J. Yang and X. Xiang, *J. Energy Chem.*, 2018, **27**, 343–350.

57 Y. Xie, Y. Li, Z. Huang, J. Zhang, X. Jia, X.-S. Wang and J. Ye, *Appl. Catal., B*, 2020, **265**, 118581.

58 J. Tian, D. Wang, S. Li, Y. Pei, M. Qiao, Z. H. Li, J. Zhang and B. Zong, *ACS Sustainable Chem. Eng.*, 2020, **8**, 594–603.

59 W. Hou, Y. Li, S. Ouyang, H. Chen, J. Ye, X. Han and Y. Deng, *Chem. Commun.*, 2019, **55**, 13279–13282.

60 J. Cao, H. Wang, Y. Zhao, Y. Liu, Q. Wu, H. Huang, M. Shao, Y. Liu and Z. Kang, *J. Mater. Chem. A*, 2020, **8**, 3701–3707.

61 L. Zhou, J. Feng, B. Qiu, Y. Zhou, J. Lei, M. Xing, L. Wang, Y. Zhou, Y. Liu and J. Zhang, *Appl. Catal., B*, 2020, **267**, 118396.

62 C. Zhang, J. Bai, L. Ma, Y. Lv, F. Wang, X. Zhang, X. Yuan and S. Hu, *Diamond Relat. Mater.*, 2018, **87**, 215–222.

63 G.-H. Moon, M. Fujitsuka, S. Kim, T. Majima, X. Wang and W. Choi, *ACS Catal.*, 2017, **7**, 2886–2895.

64 S. Kim, G.-H. Moon, H. Kim, Y. Mun, P. Zhang, J. Lee and W. Choi, *J. Catal.*, 2018, **357**, 51–58.

65 Y. Shiraishi, Y. Kofuji, H. Sakamoto, S. Tanaka, S. Ichikawa and T. Hirai, *ACS Catal.*, 2015, **5**, 3058–3066.

66 H. Ou, P. Yang, L. Lin, M. Anpo and X. Wang, *Angew. Chem., Int. Ed.*, 2017, **56**, 10905–10910.

67 Y. Yang, Z. Zeng, G. Zeng, D. Huang, R. Xiao, C. Zhang, C. Zhou, W. Xiong, W. Wang, M. Cheng, W. Xue, H. Guo, X. Tang and D. He, *Appl. Catal., B*, 2019, **258**, 117956.

68 L. Yang, G. Dong, D. L. Jacobs, Y. Wang, L. Zang and C. Wang, *J. Catal.*, 2017, **352**, 274–281.

69 Y. Zheng, Z. Yu, H. Ou, A. M. Asiri, Y. Chen and X. Wang, *Adv. Funct. Mater.*, 2018, **28**, 1705407.

70 Y. Liu, X. Zeng, X. Hu, J. Hu and X. Zhang, *J. Chem. Technol. Biotechnol.*, 2019, **94**, 22–37.

71 F. Xue, Y. Si, M. Wang, M. Liu and L. Guo, *Nano Energy*, 2019, **62**, 823–831.

72 J. Cai, J. Huang, S. Wang, J. Iocozzia, Z. Sun, J. Sun, Y. Yang, Y. Lai and Z. Lin, *Adv. Mater.*, 2019, **31**, 1806314.

73 T. Su, Q. Shao, Z. Qin, Z. Guo and Z. Wu, *ACS Catal.*, 2018, **8**, 2253–2276.

74 Q. Lu, Y. Yu, Q. Ma, B. Chen and H. Zhang, *Adv. Mater.*, 2016, **28**, 1917–1933.

75 X. Hu, X. Zeng, Y. Liu, J. Lu, S. Yuan, Y. Yin, J. Hu, D. T. McCarthy and X. Zhang, *Appl. Catal., B*, 2020, **268**, 118466.

76 Y. Shiraishi, S. Kanazawa, Y. Kofuji, H. Sakamoto, S. Ichikawa, S. Tanaka and T. Hirai, *Angew. Chem., Int. Ed.*, 2014, **53**, 13454–13459.

77 Y. Yang, G. Zeng, D. Huang, C. Zhang, D. He, C. Zhou, W. Wang, W. Xiong, X. Li, B. Li, W. Dong and Y. Zhou, *Appl. Catal., B*, 2020, **272**, 118970.

78 X. Zeng, Y. Liu, Y. Kang, Q. Li, Y. Xia, Y. Zhu, H. Hou, M. H. Uddin, T. R. Gengenbach, D. Xia, C. Sun, D. T. McCarthy, A. Deletic, J. Yu and X. Zhang, *ACS Catal.*, 2020, **10**, 3697–3706.

79 C. Chu, Q. Zhu, Z. Pan, S. Gupta, D. Huang, Y. Du, S. Weon, Y. Wu, C. Muhich, E. Stavitski, K. Domen and J.-H. Kim, *Proc. Natl. Acad. Sci. U. S. A.*, 2020, **117**, 6376.

80 Q. Zhu, Z. Pan, S. Hu and J.-H. Kim, *ACS Appl. Energy Mater.*, 2019, **2**, 7972–7979.

81 F. Yu, Y. Wang, H. Ma and G. Dong, *Int. J. Hydrogen Energy*, 2018, **43**, 19500–19509.

82 J. Xiong, X. Li, J. Huang, X. Gao, Z. Chen, J. Liu, H. Li, B. Kang, W. Yao and Y. Zhu, *Appl. Catal., B*, 2020, **266**, 118602.

83 Y. Kofuji, Y. Isobe, Y. Shiraishi, H. Sakamoto, S. Ichikawa, S. Tanaka and T. Hirai, *ChemCatChem*, 2018, **10**, 2070–2077.

84 K. Nakada, M. Fujita, G. Dresselhaus and M. S. Dresselhaus, *Phys. Rev. B: Condens. Matter Mater. Phys.*, 1996, **54**, 17954–17961.

85 Ç. Ö. Girit, J. C. Meyer, R. Erni, M. D. Rossell, C. Kisielowski, L. Yang, C.-H. Park, M. F. Crommie, M. L. Cohen, S. G. Louie and A. Zettl, *Science*, 2009, **323**, 1705–1708.

86 J.-H. Zhong, J. Zhang, X. Jin, J.-Y. Liu, Q. Li, M.-H. Li, W. Cai, D.-Y. Wu, D. Zhan and B. Ren, *J. Am. Chem. Soc.*, 2014, **136**, 16609–16617.

87 M. J. Allen, V. C. Tung and R. B. Kaner, *Chem. Rev.*, 2010, **110**, 132–145.

88 L. Han, Y. Sun, S. Li, C. Cheng, C. E. Halbig, P. Feicht, J. L. Hübner, P. Strasser and S. Eigler, *ACS Catal.*, 2019, **9**, 1283–1288.

89 P. Su, M. Zhou, X. Lu, W. Yang, G. Ren and J. Cai, *Appl. Catal., B*, 2019, **245**, 583–595.

90 W.-C. Hou and Y.-S. Wang, *ACS Sustainable Chem. Eng.*, 2017, **5**, 2994–3001.

91 L. Zheng, J. Zhang, Y. H. Hu and M. Long, *J. Phys. Chem. C*, 2019, **123**, 13693–13701.

92 L. Zheng, H. Su, J. Zhang, L. S. Walekar, H. Vafaei Molamahmood, B. Zhou, M. Long and Y. H. Hu, *Appl. Catal., B*, 2018, **239**, 475–484.

93 G.-H. Moon, W. Kim, A. D. Bokare, N.-E. Sung and W. Choi, *Energy Environ. Sci.*, 2014, **7**, 4023–4028.

94 J. Xu, Z. Chen, H. Zhang, G. Lin, H. Lin, X. Wang and J. Long, *Sci. Bull.*, 2017, **62**, 610–618.

95 X. Zeng, Z. Wang, G. Wang, T. R. Gengenbach, D. T. McCarthy, A. Deletic, J. Yu and X. Zhang, *Appl. Catal., B*, 2017, **218**, 163–173.

96 X. Zeng, Z. Wang, N. Meng, D. T. McCarthy, A. Deletic, J.-H. Pan and X. Zhang, *Appl. Catal., B*, 2017, **202**, 33–41.

97 H.-I. Kim, O. S. Kwon, S. Kim, W. Choi and J.-H. Kim, *Energy Environ. Sci.*, 2016, **9**, 1063–1073.

98 C. H. Choi, M. W. Chung, H. C. Kwon, S. H. Park and S. I. Woo, *J. Mater. Chem. A*, 2013, **1**, 3694–3699.

99 J. F. Carneiro, M. J. Paulo, M. Siaj, A. C. Tavares and M. R. V. Lanza, *J. Catal.*, 2015, **332**, 51–61.

100 Z. Zhang, H. Meng, Y. Wang, L. Shi, X. Wang and S. Chai, *Electrochim. Acta*, 2018, **260**, 112–120.

101 T.-P. Fellinger, F. Hasché, P. Strasser and M. Antonietti, *J. Am. Chem. Soc.*, 2012, **134**, 4072–4075.

102 D. Iglesias, A. Giuliani, M. Melchionna, S. Marchesan, A. Criado, L. Nasi, M. Bevilacqua, C. Tavagnacco, F. Vizza, M. Prato and P. Fornasiero, *Chem*, 2018, **4**, 106–123.

103 R. Ma, L. Wang, H. Wang, Z. Liu, M. Xing, L. Zhu, X. Meng and F.-S. Xiao, *Appl. Catal., B*, 2019, **244**, 594–603.

104 C. Zhu, M. Zhu, Y. Sun, Y. Zhou, J. Gao, H. Huang, Y. Liu and Z. Kang, *ACS Appl. Energy Mater.*, 2019, **2**, 8737–8746.

105 T. Lee, H. T. Bui, J. Yoo, M. Ra, S. H. Han, W. Kim and W. Kwon, *ACS Appl. Mater. Interfaces*, 2019, **11**, 41196–41203.

106 X. Zhang, J. Fu, Y. Zhang and L. Lei, *Sep. Purif. Technol.*, 2008, **64**, 116–123.

107 H. Zhao, Y. Chen, Q. Peng, Q. Wang and G. Zhao, *Appl. Catal., B*, 2017, **203**, 127–137.

108 Y. Liu, X. Quan, X. Fan, H. Wang and S. Chen, *Angew. Chem., Int. Ed.*, 2015, **54**, 6837–6841.

109 J. Zhang, G. Zhang, S. Jin, Y. Zhou, Q. Ji, H. Lan, H. Liu and J. Qu, *Carbon*, 2020, **163**, 154–161.

110 S. Mavrikis, M. Göltz, S. Rosiwal, L. Wang and C. Ponce de León, *ACS Appl. Energy Mater.*, 2020, **3**, 3169–3173.

111 J. Park, Y. Nabae, T. Hayakawa and M.-A. Kakimoto, *ACS Catal.*, 2014, **4**, 3749–3754.

112 X. Sheng, N. Daems, B. Geboes, M. Kurttepeli, S. Bals, T. Breugelmans, A. Hubin, I. F. J. Vankelecom and P. P. Pescarmona, *Appl. Catal., B*, 2015, **176–177**, 212–224.

113 K. Zhao, Y. Su, X. Quan, Y. Liu, S. Chen and H. Yu, *J. Catal.*, 2018, **357**, 118–126.

114 Y. Sun, I. Sinev, W. Ju, A. Bergmann, S. Dresp, S. Kühl, C. Spöri, H. Schmies, H. Wang, D. Bernsmeier, B. Paul, R. Schmack, R. Kraehnert, B. Roldan Cuenya and P. Strasser, *ACS Catal.*, 2018, **8**, 2844–2856.

115 J. O. Thostenson, E. Ngaboyamahina, K. L. Sellgren, B. T. Hawkins, J. R. Piascik, E. J. D. Klem, C. B. Parker, M. A. Deshusses, B. R. Stoner and J. T. Glass, *ACS Appl. Mater. Interfaces*, 2017, **9**, 16610–16619.

116 Y.-H. Lee, F. Li, K.-H. Chang, C.-C. Hu and T. Ohsaka, *Appl. Catal., B*, 2012, **126**, 208–214.

117 S. Chen, Z. Chen, S. Siahrostami, T. R. Kim, D. Nordlund, D. Sokaras, S. Nowak, J. W. F. To, D. Higgins, R. Sinclair, J. K. Nørskov, T. F. Jaramillo and Z. Bao, *ACS Sustainable Chem. Eng.*, 2018, **6**, 311–317.

118 C. J. Shearer, A. Cherevan and D. Eder, *Adv. Mater.*, 2014, **26**, 2295–2318.

119 M. Melchionna, P. Fornasiero and M. Prato, *Adv. Mater.*, 2019, **31**, 1802920.

120 D. Guo, R. Shibuya, C. Akiba, S. Saji, T. Kondo and J. Nakamura, *Science*, 2016, **351**, 361.

121 R. A. Sidik, A. B. Anderson, N. P. Subramanian, S. P. Kumaraguru and B. N. Popov, *J. Phys. Chem. B*, 2006, **110**, 1787–1793.

122 Y. Zhu, S. Qiu, F. Deng, F. Ma and Y. Zheng, *Sci. Total Environ.*, 2020, **722**, 137853.

123 X. Lu, D. Wang, K.-H. Wu, X. Guo and W. Qi, *J. Colloid Interface Sci.*, 2020, **573**, 376–383.

124 Y. Liu, Y. Zhao, Y. Sun, J. Cao, H. Wang, X. Wang, H. Huang, M. Shao, Y. Liu and Z. Kang, *Appl. Catal., B*, 2020, **270**, 118875.

125 A. R. Khataee, M. Safarpour, M. Zarei and S. Aber, *J. Electroanal. Chem.*, 2011, **659**, 63–68.

126 R. Pandiyan, N. Delegan, A. Dirany, P. Drogui and M. A. El Khakani, *Carbon*, 2015, **94**, 988–995.

127 L. Wang, Y. Zhang, L. Chen, H. Xu and Y. Xiong, *Adv. Mater.*, 2018, **30**, 1801955.

128 J. Sun and Y. Wu, *Angew. Chem., Int. Ed.*, 2020, **59**, 10904–10908.

129 M. Jakešová, D. H. Apaydin, M. Sytnyk, K. Oppelt, W. Heiss, N. S. Sariciftci and E. D. Głowacki, *Adv. Funct. Mater.*, 2016, **26**, 5248–5254.

130 M. K. Węcławski, M. Jakešová, M. Charyton, N. Demitri, B. Koszarna, K. Oppelt, S. Sariciftci, D. T. Gryko and E. D. Głowacki, *J. Mater. Chem. A*, 2017, **5**, 20780–20788.

131 L. Chen, L. Wang, Y. Wan, Y. Zhang, Z. Qi, X. Wu and H. Xu, *Adv. Mater.*, 2020, **32**, 1904433.

132 E. Miglbauer, M. Gryszel and E. D. Głowacki, *Green Chem.*, 2020, **22**, 673–677.

133 V. Briega-Martos, A. Ferre-Vilaplana, A. de la Peña, J. L. Segura, F. Zamora, J. M. Feliu and E. Herrero, *ACS Catal.*, 2017, **7**, 1015–1024.

134 W. Fan, B. Zhang, X. Wang, W. Ma, D. Li, Z. Wang, M. Dupuis, J. Shi, S. Liao and C. Li, *Energy Environ. Sci.*, 2020, **13**, 238–245.

135 D. Geng, Y. Chen, Y. Chen, Y. Li, R. Li, X. Sun, S. Ye and S. Knights, *Energy Environ. Sci.*, 2011, **4**, 760–764.

136 L. Qu, Y. Liu, J.-B. Baek and L. Dai, *ACS Nano*, 2010, **4**, 1321–1326.

137 K. Gong, F. Du, Z. Xia, M. Durstock and L. Dai, *Science*, 2009, **323**, 760.

138 Y. Li, W. Zhou, H. Wang, L. Xie, Y. Liang, F. Wei, J.-C. Idrobo, S. J. Pennycook and H. Dai, *Nat. Nanotechnol.*, 2012, **7**, 394–400.

139 H. T. Chung, J. H. Won and P. Zelenay, *Nat. Commun.*, 2013, **4**, 1922.

140 Y. Liang, Y. Li, H. Wang, J. Zhou, J. Wang, T. Regier and H. Dai, *Nat. Mater.*, 2011, **10**, 780–786.

141 Z. Chen, S. Chen, S. Siahrostami, P. Chakthranont, C. Hahn, D. Nordlund, S. Dimosthenis, J. K. Nørskov, Z. Bao and T. F. Jaramillo, *React. Chem. Eng.*, 2017, **2**, 239–245.

142 C. Xia, S. Back, S. Ringe, K. Jiang, F. Chen, X. Sun, S. Siahrostami, K. Chan and H. Wang, *Nat. Catal.*, 2020, **3**, 125–134.

143 M. F. Easton, A. G. Mitchell and W. F. K. Wynne-Jones, *Trans. Faraday Soc.*, 1952, **48**, 796–801.

144 S. Sorcar, Y. Hwang, C. A. Grimes and S.-I. In, *Mater. Today*, 2017, **20**, 507–515.

145 X. Li, Y. Sun, J. Xu, Y. Shao, J. Wu, X. Xu, Y. Pan, H. Ju, J. Zhu and Y. Xie, *Nat. Energy*, 2019, **4**, 690–699.

146 R. Ma, G. Lin, Y. Zhou, Q. Liu, T. Zhang, G. Shan, M. Yang and J. Wang, *npj Comput. Mater.*, 2019, **5**, 78.

147 Z. W. Seh, J. Kibsgaard, C. F. Dickens, I. Chorkendorff, J. K. Nørskov and T. F. Jaramillo, *Science*, 2017, **355**, eaad4998.

148 Z. Liu, X. Sheng, D. Wang and X. Feng, *iScience*, 2019, **17**, 67–73.

149 Q. Zhang, M. Zhou, G. Ren, Y. Li, Y. Li and X. Du, *Nat. Commun.*, 2020, **11**, 1731.

150 Y. Isaka, Y. Kawase, Y. Kuwahara, K. Mori and H. Yamashita, *Angew. Chem., Int. Ed.*, 2019, **58**, 5402–5406.